



**AFRL-RX-WP-TP-2012-0394**

**EFFECT OF SPECIMEN THICKNESS ON THE CREEP  
RESPONSE OF A Ni-BASED SINGLE CRYSTAL  
SUPERALLOY (PREPRINT)**

**A. Srivastava, S. Gopagoni, A. Needleman, and R. Banerjee**  
**University of North Texas**

**V. Seetharaman and A. Staroselsky**  
**Pratt & Whitney**

**AUGUST 2012**  
**Interim**

**Approved for public release; distribution unlimited.**

*See additional restrictions described on inside pages*

**STINFO COPY**

**AIR FORCE RESEARCH LABORATORY  
MATERIALS AND MANUFACTURING DIRECTORATE  
WRIGHT-PATTERSON AIR FORCE BASE, OH 45433-7750  
AIR FORCE MATERIEL COMMAND  
UNITED STATES AIR FORCE**

REPORT DOCUMENTATION PAGE					Form Approved OMB No. 0704-0188	
<p>The public reporting burden for this collection of information is estimated to average 1 hour per response, including the time for reviewing instructions, searching existing data sources, gathering and maintaining the data needed, and completing and reviewing the collection of information. Send comments regarding this burden estimate or any other aspect of this collection of information, including suggestions for reducing this burden, to Department of Defense, Washington Headquarters Services, Directorate for Information Operations and Reports (0704-0188), 1215 Jefferson Davis Highway, Suite 1204, Arlington, VA 22202-4302. Respondents should be aware that notwithstanding any other provision of law, no person shall be subject to any penalty for failing to comply with a collection of information if it does not display a currently valid OMB control number. <b>PLEASE DO NOT RETURN YOUR FORM TO THE ABOVE ADDRESS.</b></p>						
1. REPORT DATE (DD-MM-YY) August 2012		2. REPORT TYPE Technical Paper		3. DATES COVERED (From - To) 1 July 2012 – 1 August 2012		
4. TITLE AND SUBTITLE EFFECT OF SPECIMEN THICKNESS ON THE CREEP RESPONSE OF A Ni-BASED SINGLE CRYSTAL SUPERALLOY (PREPRINT)				5a. CONTRACT NUMBER FA8650-08-C-5226		
				5b. GRANT NUMBER		
				5c. PROGRAM ELEMENT NUMBER 62102F		
6. AUTHOR(S) A. Srivastava, S. Gopagoni, A. Needleman, and R. Banerjee (University of North Texas) V. Seetharaman and A. Staroselsky (Pratt & Whitney)				5d. PROJECT NUMBER 4347		
				5e. TASK NUMBER		
				5f. WORK UNIT NUMBER X06B		
7. PERFORMING ORGANIZATION NAME(S) AND ADDRESS(ES) University of North Texas Corner of Ave C Chestnut Denton, TX 76203				8. PERFORMING ORGANIZATION REPORT NUMBER AFRL-RX-WP-TP-2012-0394		
9. SPONSORING/MONITORING AGENCY NAME(S) AND ADDRESS(ES) Air Force Research Laboratory Materials and Manufacturing Directorate Wright-Patterson Air Force Base, OH 45433-7750 Air Force Materiel Command United States Air Force				10. SPONSORING/MONITORING AGENCY ACRONYM(S) AFRL/RXCM		
				11. SPONSORING/MONITORING AGENCY REPORT NUMBER(S) AFRL-RX-WP-TP-2012-0394		
12. DISTRIBUTION/AVAILABILITY STATEMENT Approved for public release; distribution unlimited. Preprint to be submitted to Acta Materialia.						
13. SUPPLEMENTARY NOTES This work was funded in whole or in part by Department of the Air Force contract FA8650-08-C-5226. The U.S. Government has for itself and others acting on its behalf an unlimited, paid-up, nonexclusive, irrevocable worldwide license to use, modify, reproduce, release, perform, display, or disclose the work by or on behalf of the U.S. Government. PA Case Number and clearance date: 88ABW-2012-2171, 11 April 2012. This document contains color.						
14. ABSTRACT Creep tests on Ni-based single crystal superalloy sheet specimens typically show greater creep strain rates and/or reduced strain or time to creep rupture for thinner specimens than predicted by current theories which predict a size independent creep strain rate and creep rupture strain. This size dependent creep response is termed the thickness debit effect. To investigate the mechanism of the thickness debit effect, isothermal, constant nominal stress creep tests were performed on uncoated PWA1484 Ni-based single crystal superalloy sheet specimens of thicknesses 3.18mm and 0.51mm under two test conditions: 760°C/758MPa and 982°C/248MPa. The specimens contained initial micro-voids formed during the solidification and homogenization processes. The dependence of the creep response on specimen thickness differed under the two test conditions: at 760°C/758MPa there was a reduction in the creep strain and the time to rupture with decreasing section thickness while at 982°C/248MPa a decreased thickness resulted in an increased creep rate even at low strain levels and a decreased time to rupture but with no systematic dependence of the creep...						
15. SUBJECT TERMS creep; creep damage; nickel-based single crystal superalloys; oxidation; dynamic recrystallization; lode parameter						
16. SECURITY CLASSIFICATION OF:			17. LIMITATION OF ABSTRACT: SAR	NUMBER OF PAGES 32	19a. NAME OF RESPONSIBLE PERSON (Monitor) Jaimie Tiley 19b. TELEPHONE NUMBER (Include Area Code) N/A	
a. REPORT Unclassified	b. ABSTRACT Unclassified	c. THIS PAGE Unclassified				

# Effect of specimen thickness on the creep response of a Ni-based single crystal superalloy

A. Srivastava<sup>1</sup>, S. Gopagoni<sup>1</sup>, A. Needleman<sup>1</sup>, V. Seetharaman<sup>2</sup>, A. Staroselsky<sup>2</sup>, R. Banerjee<sup>1</sup>

<sup>1</sup>*Department of Materials Science and Engineering, University of North Texas, Denton, TX, USA*

<sup>2</sup>*Pratt & Whitney, 400 Main Street, East Hartford, CT 06108, USA*

---

## Abstract

Creep tests on Ni-based single crystal superalloy sheet specimens typically show greater creep strain rates and/or reduced strain or time to creep rupture for thinner specimens than predicted by current theories which predict a size independent creep strain rate and creep rupture strain. This size dependent creep response is termed the thickness debit effect. To investigate the mechanism of the thickness debit effect, isothermal, constant nominal stress creep tests were performed on uncoated PWA1484 Ni-based single crystal superalloy sheet specimens of thicknesses 3.18mm and 0.51mm under two test conditions: 760°C/758MPa and 982°C/248MPa. The specimens contained initial micro-voids formed during the solidification and homogenization processes. The dependence of the creep response on specimen thickness differed under the two test conditions: at 760°C/758MPa there was a reduction in the creep strain and the time to rupture with decreasing section thickness while at 982°C/248MPa a decreased thickness resulted in an increased creep rate even at low strain levels and a decreased time to rupture but with no systematic dependence of the creep strain to rupture on specimen thickness. For the specimens tested at 760°C/758MPa microscopic analyses revealed that the thick specimens exhibited a mixed failure mode of void growth and cleavage while the predominant failure mode for the thin specimens was cleavage. The creep specimens tested at 982°C/248MPa in air showed the development of surface oxides and a near-surface precipitate free zone. Finite element analysis revealed that the presence of the alumina layer at the free surface imposes a constraint that locally increases the stress triaxiality and changes the value of the Lode parameter (a measure of the third stress invariant). The surface cracks formed in the oxide scale were arrested by further oxidation; for a thickness of 3.18mm the failure mode was void nucleation, growth and coalescence whereas for a thickness of 0.51mm there was a mixed mode of ductile and cleavage fracture.

**Keywords:** Creep; Creep damage; Nickel-based single crystal superalloys; Oxidation; Dynamic recrystallization; Lode parameter

---

## 1. Introduction

Single crystal Ni-based superalloys were introduced in the early 1980s [1]. Since then they have been widely used in turbine aerofoils in jet engines in order to allow for increased turbine inlet gas temperatures so as to improve thermal efficiency. The desire for weight reduction and the use of advanced metal cooling schemes to improve jet engine efficiency tends to drive designs toward thinner airfoil walls [2]. Creep tests on both polycrystalline and single crystal Ni-based superalloy specimens have shown greater creep strain rates and/or reduced strain to creep rupture for thinner specimens than predicted by current theories [3–14]. This is known as the thickness debit effect. Current theories of creep deformation and rupture are expressed in terms of stress, strain, strain rate, rupture strain and rupture time, and so, for a given applied stress, predict size independent values of the creep strain rate and the creep rupture time and strain. Phrased another way, current theories predict that for a given applied force and given specimen width the creep strain rate and the creep rupture strain should scale with the specimen thickness. The understanding of creep in single crystal superalloy turbine blades is of importance for designing more reliable and fuel efficient aircraft engines.

A qualitative comparison of the thickness debit effect for conventionally cast, columnar grain and single crystal PWA1483 superalloy materials by Duhal [5] showed that the thickness debit effect is smallest for single crystals. Doner and Heckler [4, 6] investigated the thickness debit effect in single crystal CMSX-3 mini-flat specimens. Uncoated specimens with a thickness of 0.76mm tested in air at 982°C at a stress level below 275MPa exhibited a 30% reduction in the time to creep rupture as compared with specimens with a thickness of 3.18mm. On the other hand, Doner and Heckler [4, 6] observed no thickness debit effect for both aluminide coated and uncoated specimens tested in high purity argon. Hüttner et al. [13, 14] reported a thickness debit effect in the creep response of both coated and uncoated René N5 single crystal superalloy specimens at a test temperature of 980°C. In [13, 14] coated samples showed a greater thickness debit effect than the corresponding uncoated samples. Hüttner et al. [13, 14] also showed that the samples with a misorientation of about 16° showed an increased thickness debit effect as compared with  $\langle 001 \rangle$  orientated samples. Seetharaman and Cetel [11] performed creep tests on uncoated PWA1484 (see Cetel and Duhal [15]) single crystal superalloy specimens in air at four conditions: 760°C/758MPa, 871°C/413MPa, 982°C/207MPa and 982°C/248MPa. They found a moderate thickness debit effect for the high temperature low stress (982°C/248MPa) condition and a greater thickness debit effect for the low temperature high stress (760°C/758MPa) condition.

Although attention here is focused on a single crystal superalloy, similar size dependent creep behavior has been observed in a variety of materials. Cane and Townsend [16] observed the effect of section size on the creep behavior of 0.5CrMoV steel. Storesund and Tu [17] showed that the creep life of a cross-weld bar specimen (1Cr0.5Mo weldment) is a strong function of specimen diameter. Size effect on the creep properties of lead free solders under several stress levels was observed by Ueno et al. [18]. Villain et al. [19] also observed size dependent creep response on both lead free and lead containing solders. In all cases increased creep strain rates and/or reduced creep life with decreasing sample dimensions

were seen over a range of size scales similar to those for single crystal superalloy materials.

At smaller length scales, length scales of the order of tens of microns and smaller, room temperature plastic deformation size effects have received a great deal of attention both experimentally and theoretically, e.g. [20–32]. A variety of dislocation mechanisms are known to give rise to a room temperature size dependent plastic response including geometrically necessary dislocations, dislocation starvation and source truncation, e.g. [20, 26, 29–32]. Micron scale size effects at elevated temperatures have received less attention, see [33, 34].

The thickness debit effect occurs at size scales of the order of hundreds of microns to millimeters and at elevated temperatures and, although it has been widely observed, the mechanism (or mechanisms) responsible for the thickness debit effect have not been experimentally documented. The relatively larger size scale over which the thickness debit effect occurs suggests that the mechanisms leading to creep size effects can differ from those that give rise to room temperature size effects and a variety of mechanisms have been proposed as being responsible for the thickness debit effect. Baldan [9] presumed that the thickness debit effect occurs due to a damage mechanism occurring throughout the section and argued that the creep response is controlled by the crack size to section size ratio. Doner and Heckler [4, 6] suggested that the degradation in the time to creep rupture in their experiments was primarily due to environmental effects. Seetharaman and Cetel [11] considered several possible explanations including deformation constraint, cavity nucleation, growth and coalescence, environmental degradation and changes in anisotropy with section thickness. Gullickson et al. [35] assumed that the thickness debit effect observed in the creep tests of Seetharaman and Cetel [11] was due to damage occurring in a surface layer. They used a constitutive model for the nucleation and growth of voids and carried out three dimensional finite element analyses incorporating a surface damage layer. Cassenti and Staroselsky [36] modeled a mechanism involving an overstressed boundary layer created due to plastic slip and the preferential nucleation of voids or micro-cracks near surface to explain the thickness debit effect. The results for the thickness dependence of creep curves in [35, 36] were qualitatively consistent with the experimental observations. Bensch et al. [37] analyzed surface oxidation in uncoated specimens to model the thickness debit reported in [13, 14]. Their results indicated that surface oxidation could qualitatively explain the thickness debit effect in circumstances where environmental degradation is the main mechanism.

Given the variety of observations and proposed mechanisms, a further investigation of the mechanism (or mechanisms) responsible for the thickness debit effect in creep properties of single crystal superalloys is warranted. Here, we report on creep tests and the microscopic analysis of the test specimens aimed at identifying the mechanism (or mechanisms) responsible for the thickness debit effect. The tests were performed on uncoated PWA1484 single crystal superalloy sheet specimens with thicknesses of 3.18mm and 0.51mm at 760°C/758MPa and 982°C/248MPa (the same material and test conditions as in Seetharaman and Cetel [11]). Two specimens for each thickness and test condition were creep tested until rupture, while three creep tests at 982°C/248MPa were terminated after a time in the range of 30% to 70% of the time to rupture. In total eleven creep tests were conducted. We also carry out several finite element analyses to aid in interpreting the experimental results.

## 2. Material description and experimental procedure

Single crystal bars (25.4mm diameter  $\times$  228.6mm long) of PWA1484 [15, 38] alloy with nominal chemical composition of (weight percent) Co 10.0%, Cr 5.0%, Al 5.6%, Ta 8.7%, W 6.0%, Mo 2.0%, Re 3.0%, and Ni the balance were directionally solidified at Pratt & Whitney's in-house Rapid Prototype Casting Laboratory. X-ray diffraction (Laue) analysis and macro-etching were used to confirm that the bars were single crystals with a primary orientation within  $10^\circ$  of the  $[100]$  axis. These bars were subjected to a standard sequence of heat treatment cycles, viz., solution annealing at  $1316^\circ\text{C}$  ( $2400^\circ\text{F}$ ) for 2 hours in vacuum, coating diffusion heat treatment at  $1080^\circ\text{C}$  ( $1975^\circ\text{F}$ ) for 4 hours in a controlled atmosphere, and with a precipitation heat treatment at  $704^\circ\text{C}$  ( $1300^\circ\text{F}$ ) for 24 hours in air.

Creep test specimens with rectangular cross-sections having a gauge length of  $\approx 25.58\text{mm}$ , a width of  $\approx 4.75\text{mm}$  and of a thickness of either  $h = 0.51\text{mm}$  or  $h = 3.18\text{mm}$  (Fig. 1) were electro-discharge machined from the heat treated bars and ground to remove the recast layer. The creep test specimens were machined from the bulk single crystal castings to eliminate the influence of variations in secondary dendrite arm spacing, micro-segregation patterns and initial micro-voids on the creep properties as in [11]. The sheet specimens were machined such that the orientation of the specimen width was within  $\pm 2$  degrees of  $\langle 100 \rangle$  (see Fig. 1).

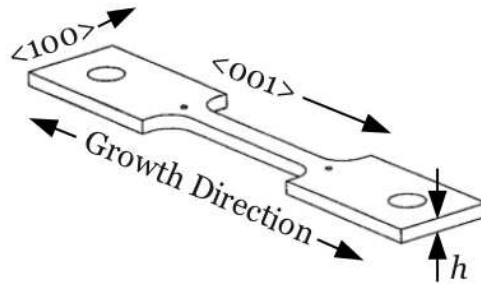


Figure 1: Schematic illustrating the shape and orientation of the uncoated PWA1484 single crystal superalloy sheet specimens used in the creep tests.

Metallographic studies were performed on all the creep tested specimens using scanning electron microscopy (SEM). Specimens creep tested in air at  $982^\circ\text{C}$  developed surface oxides where as no oxidation was observed on the specimens creep tested at  $760^\circ\text{C}$ . The chemical analysis of the oxides formed due to environmental effects during the high temperature creep tests ( $982^\circ\text{C}$ ) was performed using energy dispersive spectroscopy (EDS) in the SEM using an Apollo X silicon drift detector (SDD) at 20kV excitation voltage. The measured X-ray intensities were converted to atom% using an atomic number absorbance and fluorescence (ZAF) program. To identify the oxides formed during high temperature creep exposure, X-ray diffraction (XRD) experiments were carried out in a Rigaku Ultima III diffractometer with a Cu  $K\alpha$  ( $\lambda = 0.15406\text{nm}$ ) incident X-ray source. Electron backscatter diffraction known as orientation imaging microscopy (OIM), was carried out using a field emission gun

(FEI Nova 230) scanning electron microscope (FEGSEM) in order to determine the local texture and microstructural changes, if any.

### 3. Results

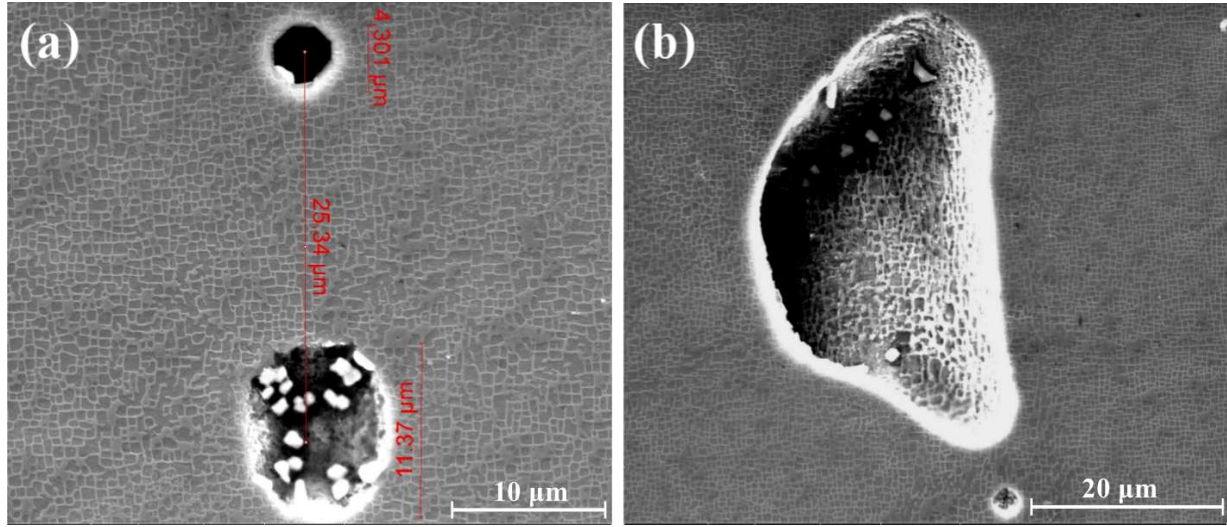


Figure 2: SEM images of the microstructure of the PWA1484 single crystal superalloy showing initial voids. (a) Two nearly spherical homogenization voids. (b) An irregular shaped shrinkage void.

The undeformed microstructure of the PWA1484 single crystal superalloy containing micro-voids is shown in Fig. 2. The microstructural characterization of the PWA1484 single crystal superalloy in the current work showed the presence of micro-voids formed during the solidification and homogenization processes as has been observed for other Ni-based single crystal superalloys (see e.g. [39, 40]). As shown in Fig. 2a the major dimension of the nearly spherical voids can exceed  $10\mu\text{m}$  while the irregular shaped voids can be even larger as in Fig. 2b where the major dimension of the irregular void is  $45\mu\text{m}$ . The nearly spherical voids are generally formed during the homogenization process and the irregular shaped voids are mainly formed during the solidification process. The volume fraction of the micro-voids is generally low but the voids are mainly confined to the interdendritic regions of the crystal which results in a relatively high local void volume fraction.

All isothermal creep tests were carried out at Metcut Research Inc., Cincinnati, OH (USA) on uncoated specimens in air under two conditions: (i) a test temperature of  $760^{\circ}\text{C}$  ( $1400^{\circ}\text{F}$ ) with a fixed nominal stress (force/initial area) of  $758\text{MPa}$  ( $110\text{ksi}$ ); and (ii) a test temperature of  $982^{\circ}\text{C}$  ( $1800^{\circ}\text{F}$ ) with a fixed nominal stress of  $248\text{MPa}$  ( $36\text{ksi}$ ). At  $760^{\circ}\text{C}$  the ratio of applied stress to yield strength is 0.79 while at  $982^{\circ}\text{C}$  this ratio is 0.46 [11]. The elastic deformation was neglected and the creep data was recorded after applying the tensile load. The creep strain ( $\epsilon_c$ ) is defined as  $\Delta\ell/\ell_0$ , where  $\ell_0$  is the initial gauge length. The creep data was recorded until a creep strain of 5% and after that the test was continued until

rupture. Based on the results of Seetharaman and Cetel [11] creep tests of two specimens of thickness 3.18mm at 982°C/248MPa were interrupted after a test duration of 75 hours ( $\varepsilon_c = 0.63\%$ ) and 145.7 hours ( $\varepsilon_c = 5.5\%$ ). For the 0.51mm thick specimens one test at 982°C/248MPa was interrupted after 51.2 hours ( $\varepsilon_c = 0.76\%$ ) to explore the evolution of damage as a function of the accumulated creep strain. Subsequently, the creep tests conducted at 760°C/758MPa will be termed the low temperature high stress creep tests and the tests at 982°C/248MPa will be termed the high temperature low stress creep tests.

### 3.1. Low temperature high stress results

#### 3.1.1. Evolution of the creep strain

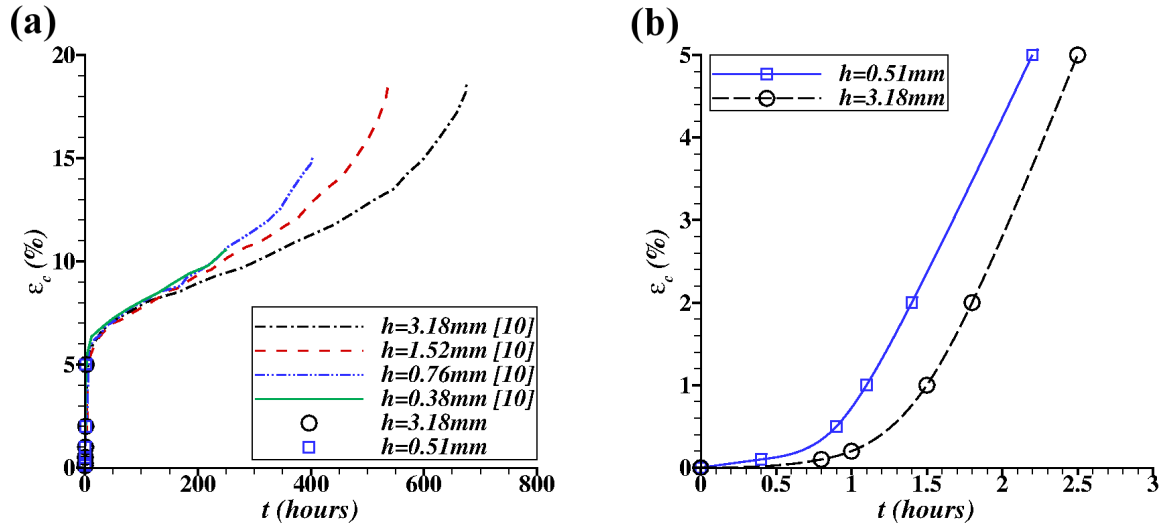


Figure 3: Creep strain,  $\varepsilon_c$  versus time,  $t$ , curves for sheet specimens having various thicknesses,  $h$ , tested at 760°C with a 758MPa applied nominal stress. (a) Data from Seetharaman and Cetel [11] and the current work are included. (b) Short time creep strain  $\varepsilon_c$  versus time,  $t$ , curves for sheet thicknesses  $h = 0.51\text{mm}$  and  $3.18\text{mm}$ .

The creep strain,  $\varepsilon_c$ , versus time,  $t$ , curves for the low temperature high stress loading condition for specimen thicknesses of 0.38mm, 0.76mm, 1.52mm and 3.18mm from the work of Seetharaman and Cetel [11] along with the results for specimen thicknesses of 0.51mm and 3.18mm from the current work are shown in Fig. 3a. Irrespective of the specimen thickness the primary creep regime extends to approximately 6% strain. The creep curves up to 5% strain for  $h = 0.51\text{mm}$  and  $h = 3.18\text{mm}$  are shown in Fig. 3b. Both specimens showed a brief incubation period (i.e. the time delay before primary creep begins) followed by a constant primary creep rate. Under similar creep loading conditions Wilson and Fuchs [41] also reported incubation period in PWA1484 single crystal superalloy. The difference in incubation period between the specimens with  $h = 3.18\text{mm}$  and those with  $h = 0.51\text{mm}$  seems to be statistical in nature and not thickness dependent, but a definite conclusion cannot be made based on the two tests conducted for each specimen thickness. Specimens



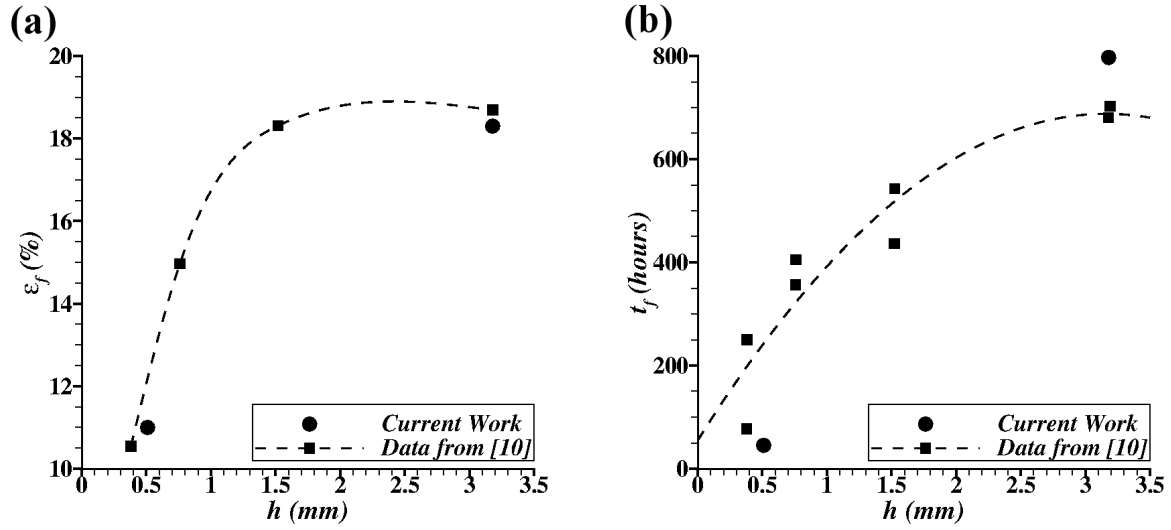


Figure 4: The effect of specimen thickness ( $h$ ) on (a) the creep strain to fracture ( $\epsilon_f$ ) and (b) the time to fracture ( $t_f$ ) of sheet specimens creep tested at 760°C/758MPa. Data from Seetharaman and Cetel [11] and the current work are included. The dotted lines, a spline in (a) and a second order polynomial in (b), are fits to show the trend of the data from [11].

of thickness 0.51mm reached 5% creep strain in 2.2 hours and those with thickness 3.18mm reached  $\epsilon_c = 5\%$  in 2.5 hours. The difference in time to 5% creep strain is very small as compared with the difference in final creep rupture time. As shown in Fig. 3a decreasing the specimen thickness from 3.18mm to 1.52mm resulted in a slight increase in steady state creep rate and showed an early inflection of the straight portion of the creep strain versus time curve. For specimens of thicknesses 0.76mm, 1.52mm and 3.18mm a deviation from the steady state creep towards tertiary creep is observed whereas no signature of tertiary creep is observed for specimens of thickness 0.38mm.

For the creep behavior shown in Fig. 3a, the creep rupture properties can be represented by creep strain to rupture i.e. creep ductility as shown in Fig. 4a. In Fig. 4a the creep strain to rupture for a specimen with thickness  $h = 0.38\text{mm}$  where no tertiary creep is observed is significantly smaller than that for the specimen with  $h = 3.18\text{mm}$  where pronounced tertiary creep is observed. As will be discussed in more detail subsequently, the reduced tertiary creep in thinner specimens is associated with a transition from creep-ductile to creep-brittle behavior for thinner specimens. As shown in Fig. 4a the strain to rupture is nearly the same for  $h = 3.18\text{mm}$  and  $h = 1.52\text{mm}$ . For thinner specimens, the creep ductility is reduced. There is a more than 40% reduction in the creep rupture strain  $\epsilon_f$  for the specimens with a thickness of 0.38mm as compared with the specimens with  $h = 3.18\text{mm}$  as seen in Fig. 4a. The time to creep rupture for specimens with various thicknesses is shown in Fig. 4b. The time to creep rupture,  $t_f$ , is reduced by about 60% for the  $h = 0.38\text{mm}$  specimens as compared with the specimens of thickness  $h = 3.18\text{mm}$ .

### 3.1.2. Fractography

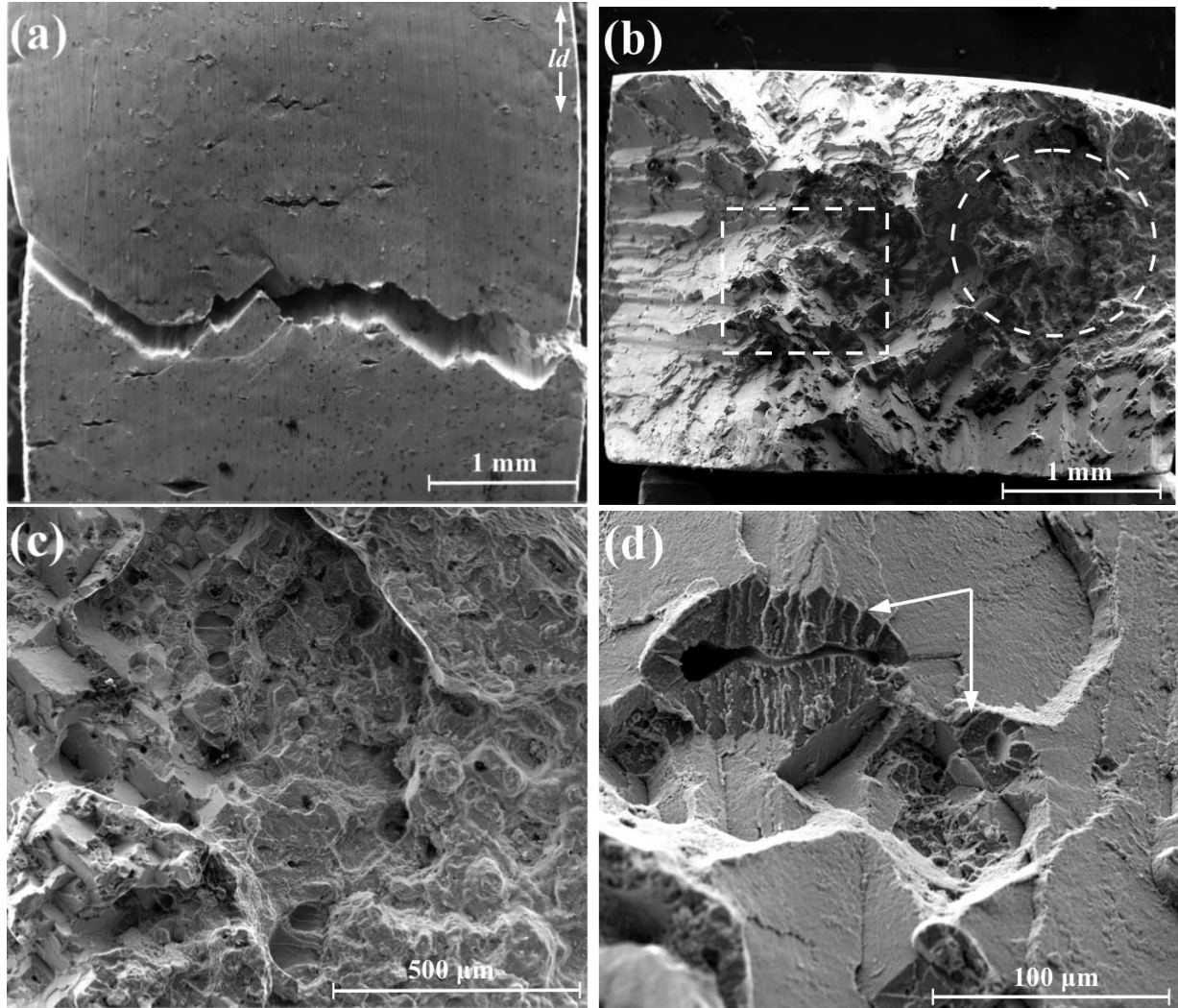


Figure 5: SEM images of a 3.18mm thick sheet specimen tested at 760°C/758MPa. (a) The region near the fracture surface reconstructed after rupture (the loading direction is  $ld$  and the sheet thickness is into the plane). (b) The fracture morphology of the upper half of the specimen in (a) (the loading direction is into the viewed plane). (c) Zoomed view of the region enclosed by the dotted circle in (b). (d) Zoomed view of the region enclosed by the dotted rectangle in (b).

To further explore the mechanism behind thickness debit effect, we performed standard fractography using secondary electron imaging (SE) in a scanning electron microscope (SEM). No surface oxidation was observed at this temperature. The reconstructed creep ruptured specimen of thickness 3.18mm is shown in Fig. 5a. The constant nominal stress creep loading direction in Fig. 5a is marked as  $ld$ . The thickness of the sheet specimen is into the plane of the image. As visible in Fig. 5a, failure of the specimen was accompanied by slight necking. The cross-sectional area near fracture surface is approximately 10% less

than the cross-sectional area of the far gauge section. Micro-cracks are also present away from the fracture region on the gauge section. The fracture surface, which is inclined to the tensile axis, can be seen in reconstructed specimen. The fracture morphology in Fig. 5b shows the stepped cleavage planes as well as micro-voids. The crystallographic cleavage planes with traces of slip bands shows creep deformation by slip process. The edges of the projected fracture surface are inclined at an angle  $\approx 45^\circ$  with respect to the loading axis i.e.  $\langle 001 \rangle$  crystallographic direction in Fig. 5a. This shows that the edges are along  $\langle 011 \rangle$  direction. It is important to note that  $\{111\}$  planes intersects with  $\{100\}$  planes along  $\langle 011 \rangle$  direction. Hence the cleavage took place on the planes subjected to maximum resolved shear stress which are the  $\{111\}$  family of planes based on the Schmid factor. Similar observations were made by Sherry and Pilkington [42] in creep rupture testing of single-crystal superalloy SRR99 at  $750^\circ\text{C}$ . The presence of numerous crystallographic facets indicate planar inhomogeneous plastic deformation. The zoomed view of the region with void activity in Fig. 5c shows numerous shallow voids joined by shear along slip bands. In the other zoomed view of the fracture surface in Fig. 5d the voids connected through micro-cracks are also seen. At several locations the fracture surface surrounding the voids is orthogonal to the loading axis as in brittle fracture (marked by arrow in Fig. 5d). Also two intersecting  $\{111\}$  crystallographic cleavage planes can be observed.

The reconstructed creep ruptured specimen of thickness  $h = 0.51\text{mm}$  is shown in Fig. 6a. The tensile creep loading direction in Fig. 6a is marked as  $ld$  and the specimen thickness is perpendicular to the plane of the image. No necking was observed in the failed specimen with  $h = 0.51\text{mm}$ . Unlike for the thicker specimen there is no evidence of micro-cracks on the surface away from the fracture region. The orthogonal view of the region marked with a dotted circle in Fig. 6a is shown in Fig. 6b. In the upper half of Fig. 6b there is a region of uneven ductile fracture. This region contains numerous micro-cracks that apparently originated from micro-voids. A shear lip inclined at an angle of approximately  $45^\circ$  to the loading axis can also be seen at the bottom of the image. The shear lip contains numerous cleavage steps. At the root of the shear lip a river pattern [43] can be seen. The fracture morphology of the region marked with a dotted rectangle in Fig. 6a is shown in Fig. 6c. This part of the fracture surface is flat with the right side edge inclined at an angle  $\approx 45^\circ$  to the loading axis, which is the  $\langle 011 \rangle$  crystallographic direction, as can be seen in the inset of the Fig. 6c. This implies that a major portion of the specimen is sheared along a single plane through the thickness. Micro-cracks and micro-voids are present on this surface. Figure 6d shows the zoomed view of the fracture surface between the dotted circle and the dotted rectangle in Fig. 6a. Here the presence of intersecting crystallographic cleavage planes shows that rupture in this region occurred along more than one  $\{111\}$  family of planes.

The SEM image of the section above the fracture surface and normal to the loading direction of the specimen with  $h = 0.51\text{mm}$  in Fig. 7 shows the presence of internal micro-cracks. The crack in Fig. 7a probably arises from the coalescence of larger shrinkage voids and smaller homogenization voids. The failure process involves the initiation and growth of cracks from the void surface as shown in Fig. 7b. Cracks such as those in Fig. 7a and 7b are also present in the specimen with  $h = 3.18\text{mm}$  at locations just above the fracture surface.

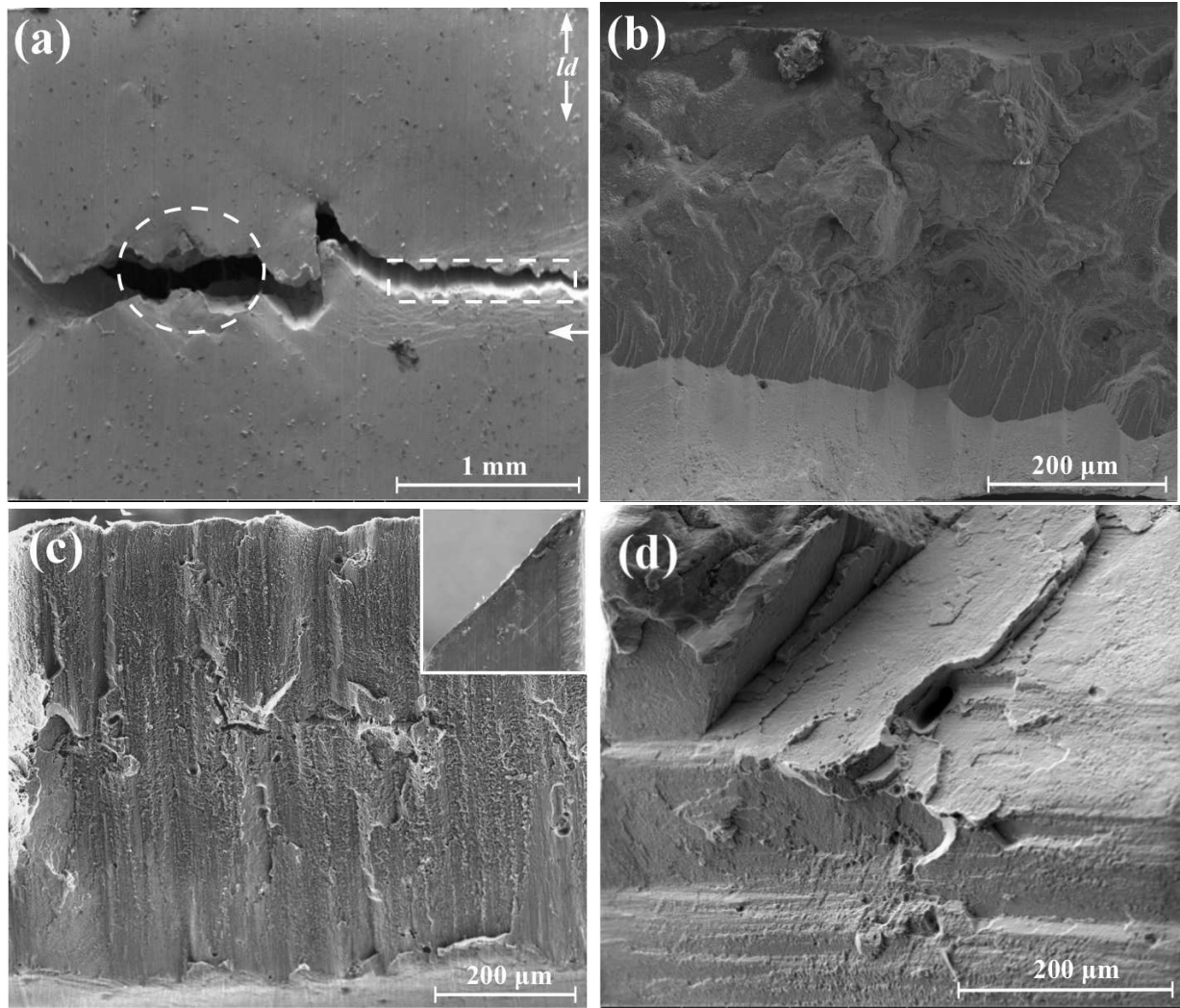


Figure 6: SEM images of a 0.51mm thick sheet specimen tested at 760°C/758MPa. (a) The region near the fracture surface reconstructed after rupture (the loading direction is  $ld$  and the sheet thickness is into the plane). (b) The fracture morphology of the region marked by a dotted circle in (a) (the loading direction is into the viewed plane). (c) The fracture morphology of the region marked by a dotted rectangle in (a) and the inset shows the side view marked by the arrow in (a). (d) Zoomed view of the fracture surface showing stepped cleavage planes.

Once a crack initiates from a void it propagates along crystallographic planes, probably  $\{111\}$  planes, that have a high resolved shear stress. The presence of the bead-like structure at the lower right end of the crack in Fig. 7b shows the presence of micro-voids connected through inter-void cleavage.

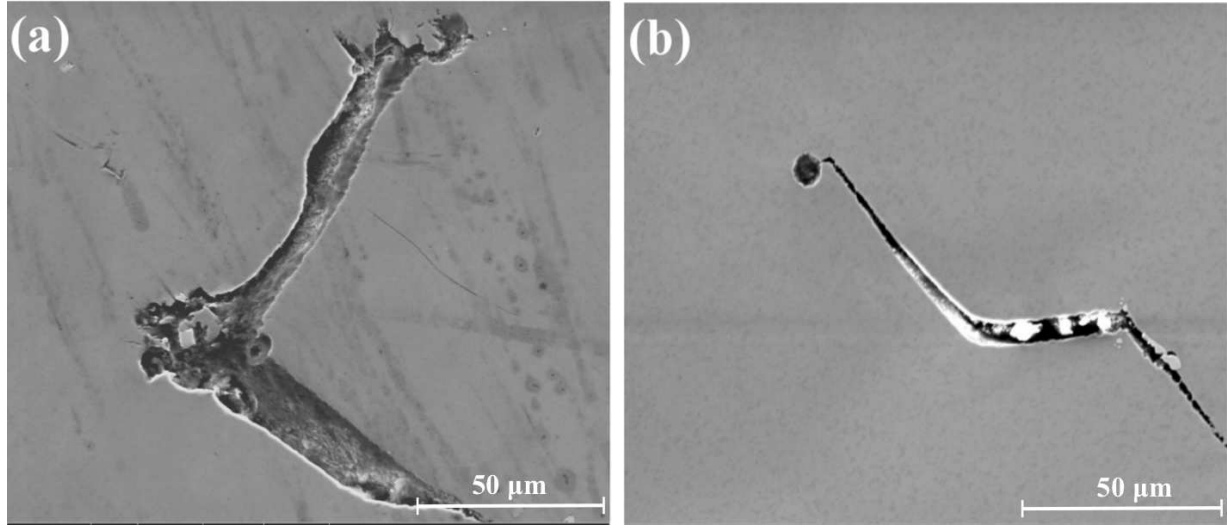


Figure 7: SEM images from the section near fracture surface of a 0.51mm thick specimen tested at 760°C/758MPa showing the presence of internal micro-cracks. (a) Initiation and growth of crack from voids close enough to coalesce. (b) Initiation and growth of crack from the surface of an isolated void.

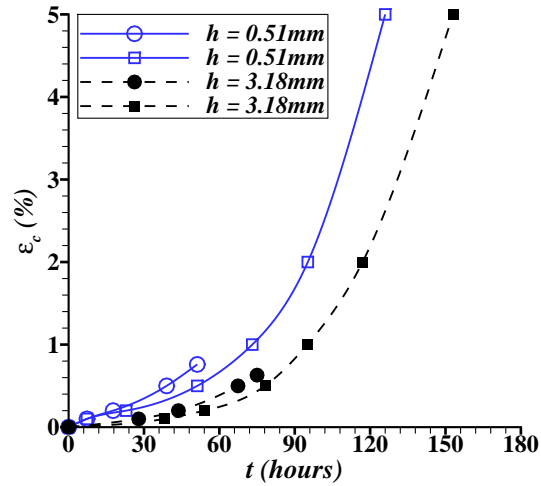


Figure 8: Creep strain ( $\varepsilon_c$ ) versus time ( $t$ ) curves for sheet specimens with  $h = 0.51\text{mm}$  and  $h = 3.18\text{mm}$  tested at 982°C and with 248MPa applied nominal stress to a creep strain of  $\varepsilon_c = 5\%$ . Also shown are creep strain versus time curves for creep tests interrupted after  $t = 51.2$  hours for  $h = 0.51\text{mm}$  and after  $t = 75$  hours for  $h = 3.18\text{mm}$ .

### 3.2. High temperature low stress results

#### 3.2.1. Evolution of the creep strain

Curves of creep strain versus time for specimen thicknesses of  $h = 0.51\text{mm}$  and  $h = 3.18\text{mm}$  tested at a temperature of 982°C and a nominal stress of 248MPa are shown in

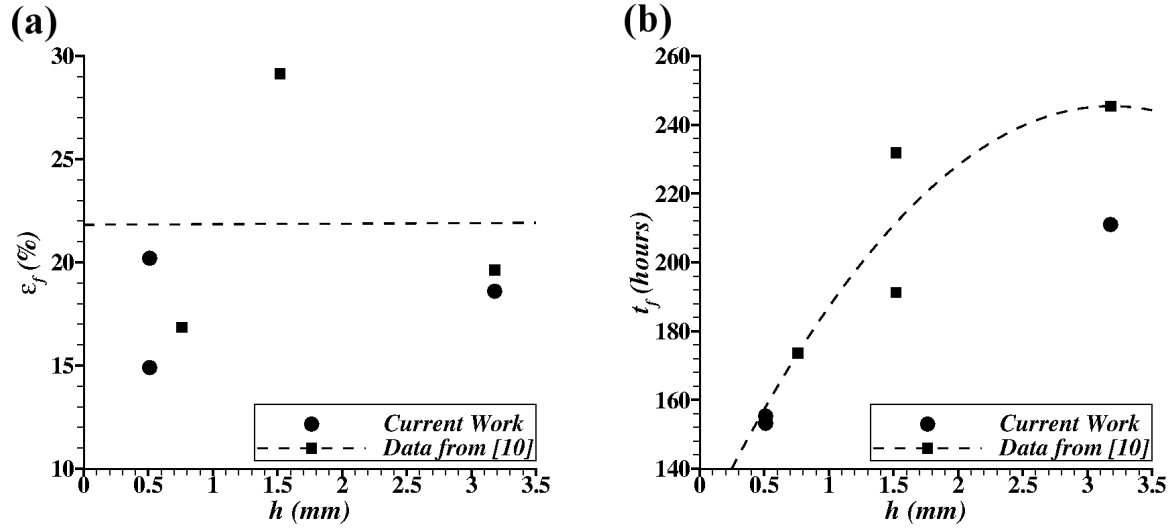


Figure 9: The effect of specimen thickness ( $h$ ) on (a) the creep strain to fracture ( $\epsilon_f$ ) and (b) the time to fracture ( $t_f$ ) for sheet specimens creep tested at 982°C/248MPa. Data from Seetharaman and Cetel [11] and the current work are included. The dotted lines, linear in (a) and a second order polynomial in (b), are fits to show the trend of the data from [11].

Fig. 8. The creep strain versus time curves were recorded until a creep strain of 5%. Two tests for each specimen thickness were continued to rupture while two tests on specimens with  $h = 3.18\text{mm}$  were interrupted after test durations of 75 hours and 145.7 hours. One test on a specimen with  $h = 0.51\text{mm}$  was interrupted after a test duration of 51.2 hours. The interrupted tests allowed exploration of the damage evolution as a function of accumulated creep strain. The negligible primary creep and absence of a well defined steady state creep region are the major differences observed at the high temperature low stress condition as compared with the low temperature high stress condition. As shown in Fig. 8 the time to reach 5% creep strain for a specimen of thickness 3.18mm is 152 hours while for a specimen of thickness 0.51mm it is 125 hours. The plots in Fig. 8 show an increased creep rate with decreasing thickness at low strain levels for both the specimens tested to rupture and for the interrupted tests.

The creep strain to rupture and the time to rupture for specimens with  $h = 0.51\text{mm}$  and with  $h = 3.18\text{mm}$  from the current work and for specimens with  $h = 0.76\text{mm}$ ,  $h = 1.52\text{mm}$  and  $h = 3.18\text{mm}$  from the work of Seetharaman and Cetel [11] are shown in Figs. 9a and 9b respectively. In contrast to the low temperature high stress creep test results, no systematic dependence of the creep strain to rupture on specimen thickness is observed. However, there is a dependence of the time to rupture on specimen thickness as shown in Fig. 9b. The specimens with thickness  $h = 3.18\text{mm}$  ruptured after 210 hours whereas the specimens with  $h = 0.51\text{mm}$  ruptured after 155 hours, a reduction of about 25% in the time to creep rupture.

### 3.2.2. Metallographic and Chemical Analysis

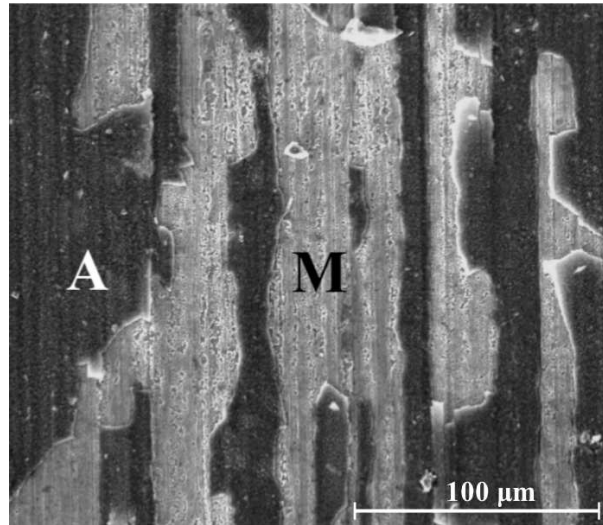


Figure 10: SEM image of the unstressed shoulder region of a specimen creep tested at 982°C/248MPa. A marks the Al-rich oxide layer and M marks the mixed oxide layer.

In contrast to the creep tests at 760°C significant surface oxidation was observed during the creep tests at 982°C. We analyzed the surface of the creep tested specimens in a SEM using secondary electron (SE) imaging. Figure 10 shows the shoulder region of the grip of the specimen where no creep deformation occurred. The image clearly shows the presence of two layers. The brighter being the top surface layer and the darker being below that layer, suggesting spallation of the brighter layer. The spallation of oxide layers at metal/alumina interface in PWA1484 superalloy has been discussed by Mennicke et al. [44] and Nychka et al. [45]. The grip region of all specimens creep tested at 982°C/248MPa show similar surfaces.

Unlike the near grip region of the creep tested specimens, the surface texture of the gauge region depends on the creep exposure time. Figures 11 and 12 shows the surface textures of the gauge region surface oxide after various creep exposure times for specimens with thicknesses  $h = 3.18\text{mm}$  and  $h = 0.51\text{mm}$  respectively. As will be shown subsequently, layer A is an Al-rich oxide layer and layer M is a mixed oxide layer. After 75 hours of creep exposure time for  $h = 3.18\text{mm}$  and 51.2 hours of creep exposure time for  $h = 0.51\text{mm}$ , the gauge region surface shows a single oxide layer marked as layer A in Figs. 11a and 12a. With continuing creep exposure after 145.7 hours as in Fig. 11b layer A on the specimen gauge surface develops cracks perpendicular to the loading direction. These cracks expose metal to air for further oxidation. The oxides formed in the open cracks are shown in Fig. 11c for  $h = 3.18\text{mm}$  and in Fig. 12b for  $h = 0.51\text{mm}$ . This shows that the surface cracks in layer A were arrested due to further oxidation.

An extensive metallographic examination of a polished sample taken from near the fracture region of the gauge section of the creep ruptured specimens showed the presence of

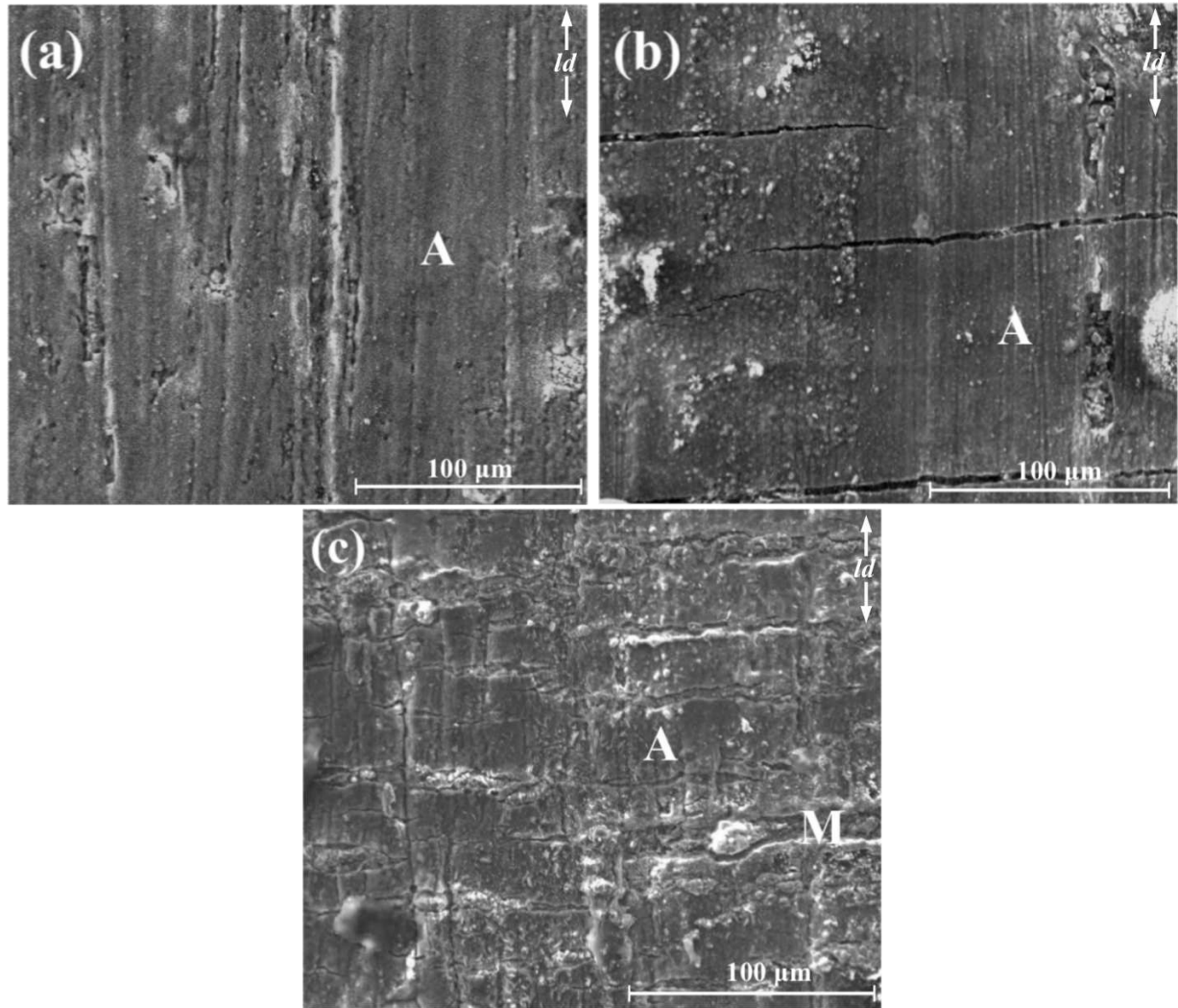


Figure 11: SEM images from the gauge region of a  $h = 3.18\text{mm}$  specimen creep tested at  $982^\circ\text{C}/248\text{MPa}$ . (a) The test interrupted after 75 hours. (b) The test interrupted after 145.7 hours. (c) A region above the fracture surface from the creep ruptured specimen (the loading direction is  $ld$ ). A marks the Al-rich oxide and M marks the mixed oxide.

various layers of oxides and the microstructure that developed in the alloy. One of the images taken from near the fracture surface of a  $3.18\text{mm}$  thick creep ruptured specimen is shown in Fig. 13. Similar layers can also be seen in  $0.51\text{mm}$  thick specimens. Here we can clearly notice three layers of oxides, a Ni-rich oxide layer (layer N), a mixed oxide layer (layer M) and an Al-rich oxide layer (layer A). The first layer after the oxide layers is a precipitate free layer, denoted as layer L1. As shown in the Fig. 13 no  $\gamma'$  precipitates are present in this layer. Two interesting features observed in layer L1 are the presence of large micro-voids and faceted precipitates (marked with an arrow). After the  $\gamma'$ -free layer is the depleted  $\gamma'$  precipitate layer, denoted as L2. The extensive rafting of  $\gamma'$  normal to the loading direction



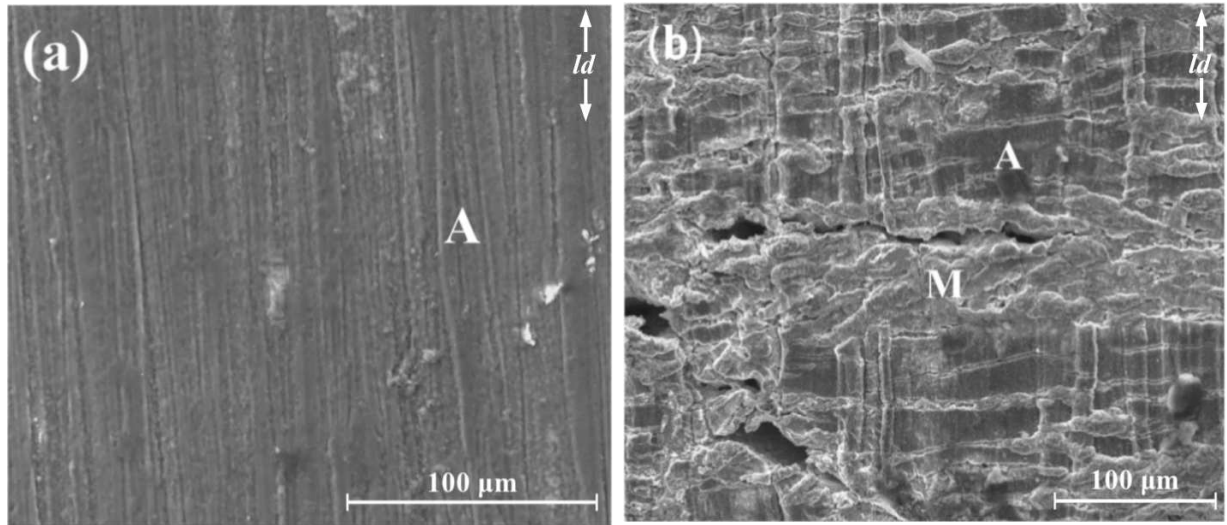


Figure 12: SEM images from the gauge region of a  $h = 0.51\text{mm}$  specimen creep tested at  $982^\circ\text{C}/248\text{MPa}$ . (a) The test interrupted after 51.2 hours. (b) A region above the fracture surface from the creep ruptured specimen (the loading direction is  $ld$ ). A marks the Al-rich oxide and M marks the mixed oxide.

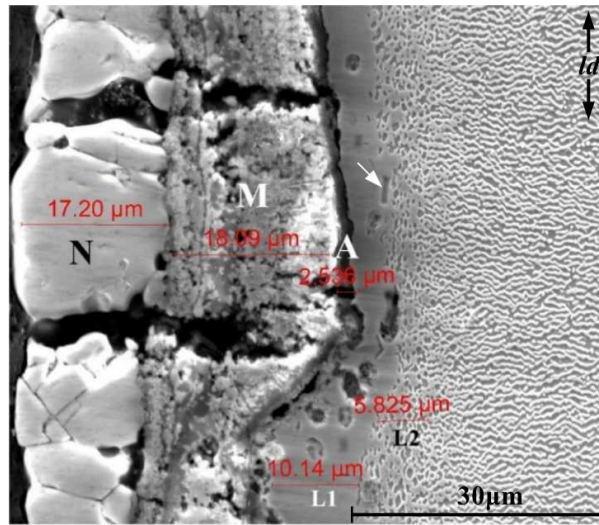


Figure 13: SEM image from near the fracture surface showing three layers of oxides in a  $h = 3.18\text{mm}$  specimen creep tested at  $982^\circ\text{C}/248\text{MPa}$ . N marks the Ni-rich oxide layer. M marks the mixed oxide layer. A marks the Al-rich oxide layer. L1 marks the  $\gamma'$  free layer. L2 marks the  $\gamma'$  reduced layer. The rafting in the bulk can be seen. The arrow marks the presence of faceted precipitates in the L1 layer. The loading direction is  $ld$ .

in the bulk of the material is consistent with other observations on superalloys characterized by a small negative misfit between the lattices of  $\gamma$  and  $\gamma'$  phases, e.g. [46].

The first two oxide layers shown in Fig. 13 are present in small patches on the specimen

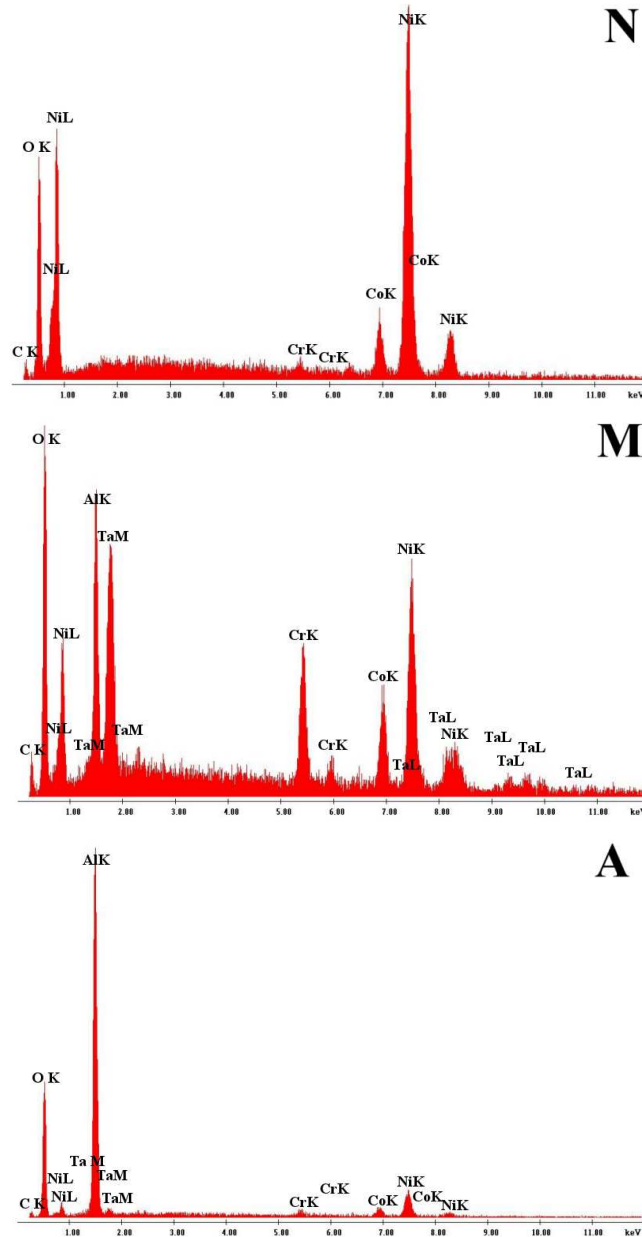


Figure 14: EDX spectra from the representative regions marked as N, M and A in Fig. 13.

surface both at stressed gauge section or unstressed grip section. The EDX spectra in Fig. 14 identifies layer N as a Ni-rich oxide layer. Extensive spallation of the Ni-rich oxide layer is also reported in [45]. Layer-M as per the EDX spectra is a mixed oxide of Ni, Al, Ta, Cr and Co. This mixed oxide layer precedes the Ni-rich oxide layer and is also present in the cracks in adherent layer A as shown in Fig. 11c and 12b. The adherent layer A is the Al-rich oxide as per EDX spectra in Fig. 14. A detailed study on the formation of alumina

scale in Ni-based single crystal superalloy can be found in the recent work of Sato et al. [47]. The quantification of EDX spectra from the faceted precipitates in the  $\gamma'$ -free layer in Fig. 13 suggests the presence of an Al-rich precipitate with the ratio of atom% of Ni and Al approximately equal to unity suggesting the formation of the  $\beta$  (NiAl) phase. Similar oxidation induced phase transformation and formation of different Al-rich precipitates are reported in the oxidation studies of CMSX-10 by Akhtar et al. [48].

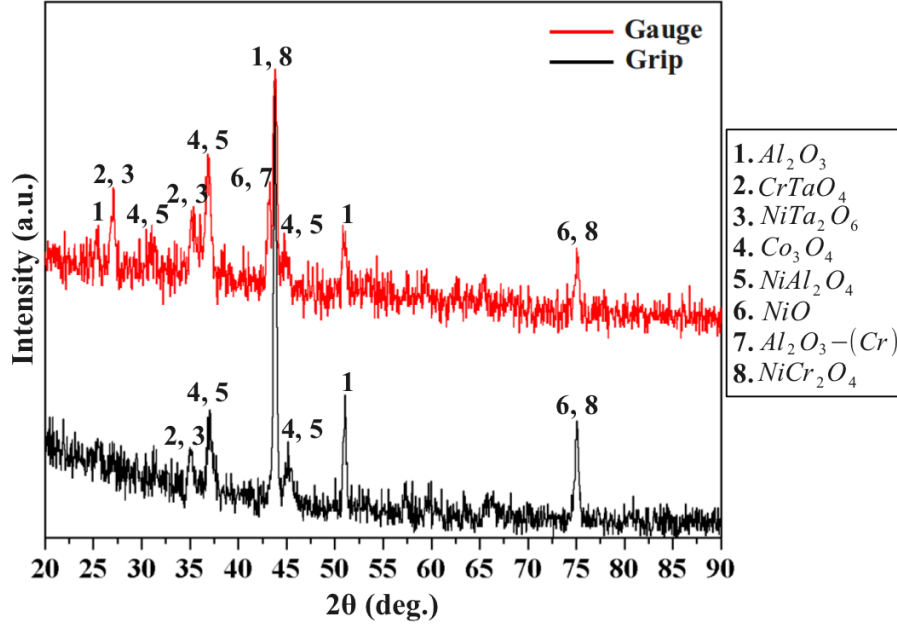


Figure 15: XRD patterns from the shoulder region of the unstressed grip section and from the near fracture region of the gauge section of a specimen creep tested at 982°C/248MPa. Intensities (in arbitrary units) are vertically offset to show the data effectively.

The XRD patterns from the grip and the gauge region of the unpolished samples creep tested at 982°C/248MPa are shown in Fig. 15. The XRD patterns in Fig. 15 reveal the formation of the various oxides and spinels namely Cr doped  $\text{Al}_2\text{O}_3$ ,  $\text{Al}_2\text{O}_3$ ,  $\text{Co}_3\text{O}_4$ , NiO,  $\text{NiTa}_2\text{O}_6$ ,  $\text{CrTaO}_4$ ,  $\text{NiAl}_2\text{O}_4$  and  $\text{NiCr}_2\text{O}_4$ . Several diffraction peaks from these oxides overlap and are shown in Fig. 15 for the sake of completeness. From the information in Figs. 13, 14 and 15 we can comment on the sequence of phase transformations occurring due to oxidation. The formation of the first external oxide layer which is predominantly NiO results in a nickel depleted region between the base alloy and the external oxide scale. This compositional shift induces a phase transformation of the ( $\gamma$ - $\gamma'$ ) base material to the Al-rich ( $\beta$  phase) precipitates in the Ni-depleted zone. With continued exposure to air at high temperature further oxidation takes place until a stable alumina layer is formed at the metal-mixed oxide interface. The alumina layer forms at the cost of  $\gamma'$  and other Al-rich precipitates (formed due to oxidation induced phase transformation) resulting in the formation of a  $\gamma'$ -free zone followed by a  $\gamma'$ -depleted zone. Such environmental degradation of the uncoated specimens creep tested at 982°C/248MPa is independent of the specimen thickness.

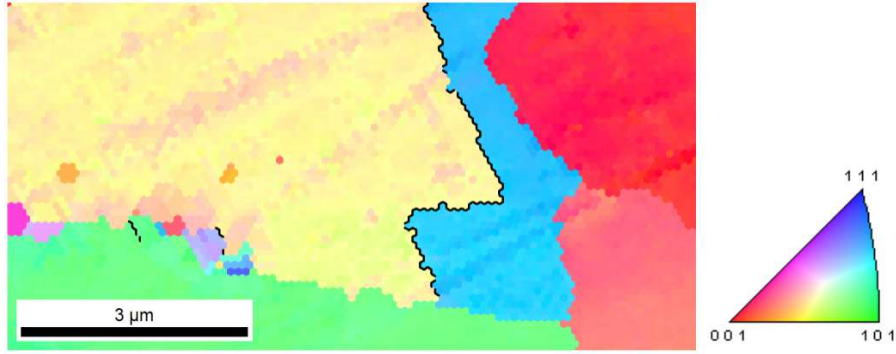


Figure 16: Inverse pole figure map of the  $\gamma'$  free zone in a specimen creep tested to fracture at 982°C/248MPa. The map is given in the [001] orientation. The recrystallized grain orientations can be seen from the color-coded stereographic triangle.  $\Sigma_3$  (twin) boundaries are marked in black.

The EBSD inverse pole figure of the  $\gamma'$  precipitate free zone in Fig. 13 is shown in Fig. 16. Figure 16 represents an area of  $9.1 \times 4.6 \mu\text{m}^2$ . The electron beam was scanned in steps of  $0.1 \mu\text{m}$  and the EBSD pattern was indexed using the nickel fcc phase. The interesting observation from the EBSD analysis is the presence of recrystallized grains. Dynamic recrystallization in the precipitate free zone under the oxide scale occurred in both the specimens of thickness  $h = 3.18\text{mm}$  and  $h = 0.51\text{mm}$ . The dynamic recrystallization mainly resulted in subgrain boundaries and recrystallization twin boundaries. The grain boundaries that formed during recrystallization could lead to creep cavitation. An increase in the number of voids in the precipitate free zone is indeed seen in Fig. 13. Hence oxidation not only contributes to a reduction in load carrying cross-sectional area but also produces a boundary layer which is prone to void nucleation. The size of the recrystallized zone formed due to oxidation during high temperature creep will be independent of the specimen thickness and will affect thin specimens more than thicker specimens.

The evolution of damage in the form of micro-voids and micro-cracks with both  $h = 0.51\text{mm}$  and  $h = 3.18\text{mm}$  is shown in Fig. 17. Figures 17a and 17b compare the accumulated damage in the gauge region of a specimen interrupted after 51.2 hours ( $\varepsilon_c=0.76\%$ ) and in the region above the fracture surface of a creep ruptured ( $\varepsilon_f=14.9\%$  and the  $t_f = 155$  hours) specimen with  $h = 0.51\text{mm}$ . The comparison reveals an increase in the number and size of micro-voids with increasing creep deformation. Several voids are elongated in the loading direction and also many voids have initiated micro-cracks (due to cleavage or coalescence) perpendicular to the loading direction. Similarly Figs. 17c and 17d compare the accumulated damage in the gauge region of a specimen interrupted after 75 hours ( $\varepsilon_c=0.63\%$ ) and in the region above fracture surface of the creep ruptured ( $\varepsilon_f=18.6\%$  and  $t_f = 210$  hours) specimen with  $h = 3.18\text{mm}$ . The increased number of voids observed after creep deformation suggests growth of existing voids as well as the nucleation of new voids. Epishin and Link [49] observed similar growth of initial voids in the interdendritic regions and nucleation of new voids at the  $\gamma$ - $\gamma'$  interfaces. A comparison of Figs. 17b and 17d shows an increased number and size of micro-voids and more micro-cracks in the creep ruptured specimen with  $h = 3.18\text{mm}$ .

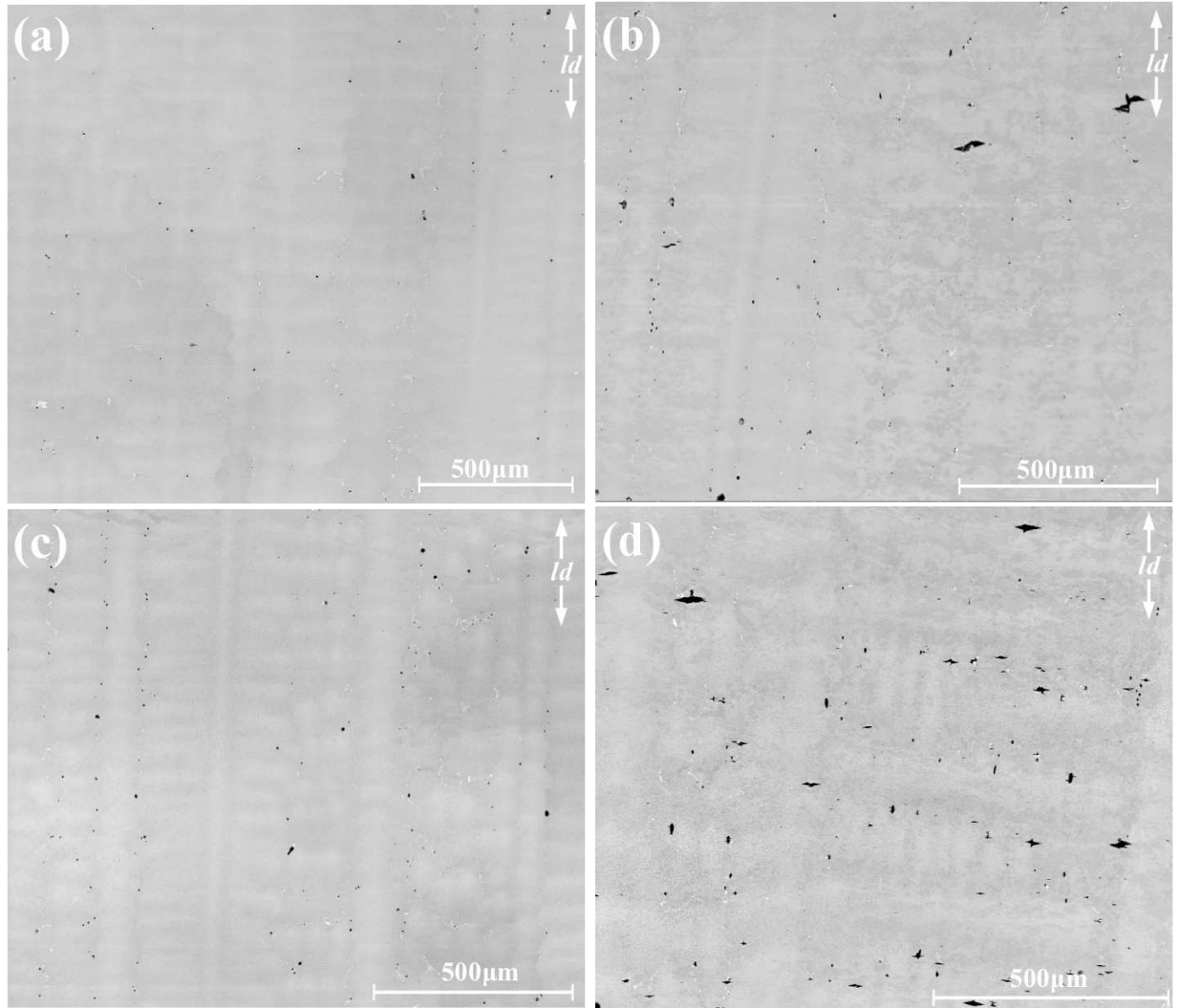


Figure 17: SEM images showing evolution of damage in the gauge region of the specimens creep tested at 982°C/248MPa. (a) A  $h = 0.51\text{mm}$  thick specimen after 51.2 hours. (b) A  $h = 0.51\text{mm}$  thick specimen after creep rupture. (c) A  $h = 3.18\text{mm}$  thick specimen after 75 hours. (d) A  $h = 3.18\text{mm}$  thick specimen after creep rupture. The loading direction is  $ld$ .

as compared with the specimen with  $h = 0.51\text{mm}$ . Link et al. [40] discussed that the deformation induced void nucleation and growth increases with time and it is worth noting that the specimen with thickness 0.51mm ruptured after 155 hours whereas the specimen with thickness 3.18mm ruptured after 210 hours.

### 3.2.3. Fractography

The SEM image of the reconstructed creep ruptured specimen with thickness  $h = 3.18\text{mm}$  is shown in Fig. 18a. The tensile loading direction is marked as  $ld$  and the thickness is into the plane of the image. No necking was observed in the failed specimen. The presence of



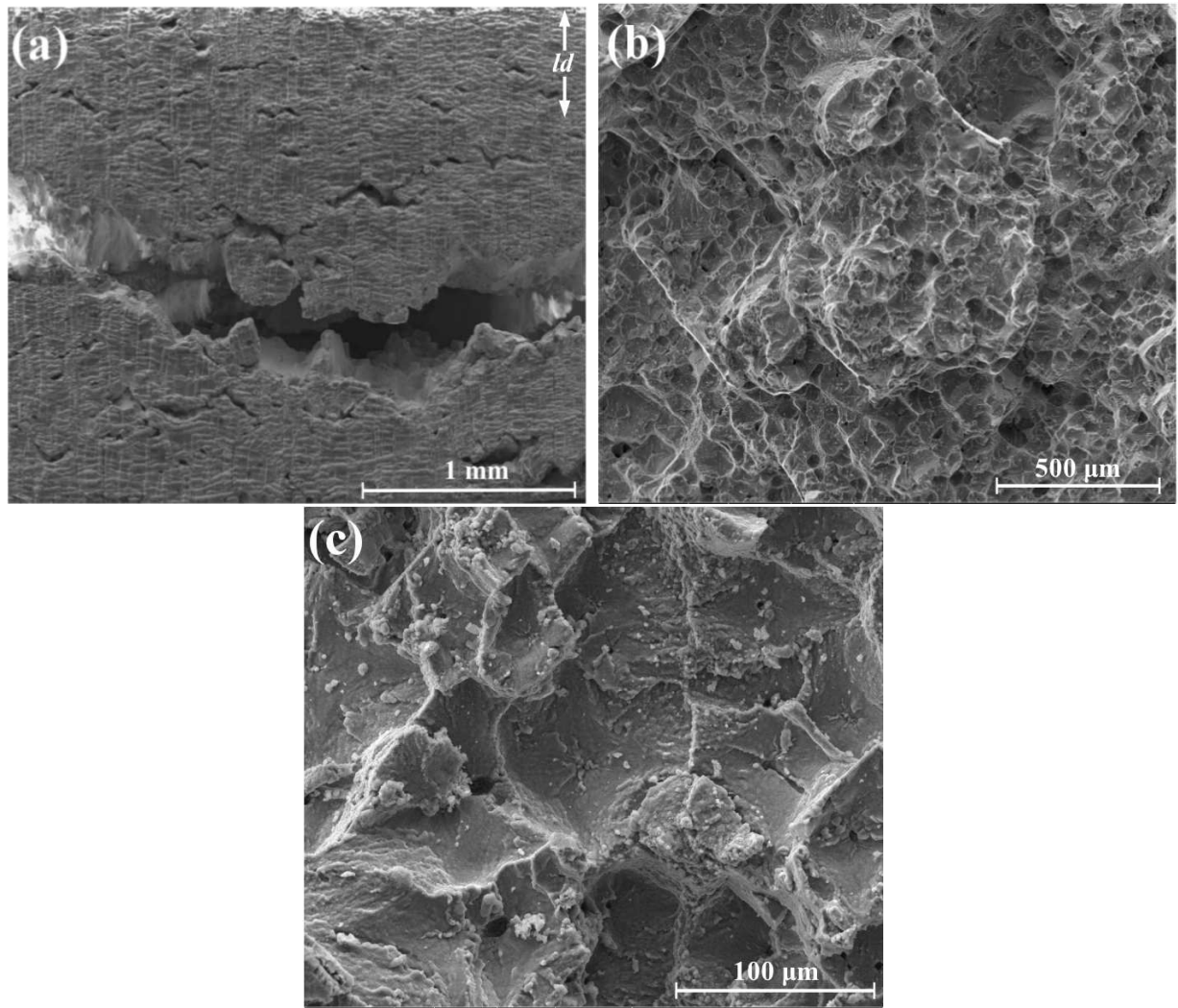


Figure 18: SEM images of a 3.18mm thick sheet specimen tested at 982°C/248MPa. (a) The region near the fracture surface reconstructed after rupture (the loading direction  $ld$  and the sheet thickness is into the plane). (b) The fracture morphology of the one half of the specimen in (a) (the loading direction is into the viewed plane). (c) Zoomed view of the fracture surface in (b).

micro-cracks perpendicular to the loading direction can be seen in the gauge section away from the fracture surface. A homogeneous fracture morphology suggesting dimple rupture can be seen in Fig. 18b. The zoomed view of the fracture morphology in Fig. 18c shows the presence of micro-voids and micro-cracks in the cup-like depressions. This suggests that the rupture occurred due to the nucleation, growth and coalescence of voids and not because of micro-cracks initiated in the oxide layer as these cracks arrested after further oxidation.

The reconstructed creep ruptured specimen of thickness  $h = 0.51\text{mm}$  is shown in Fig. 19a. The tensile loading direction is marked as  $ld$  and the thickness is into the plane of the image. No necking was observed in the failed specimen. The presence of micro-cracks

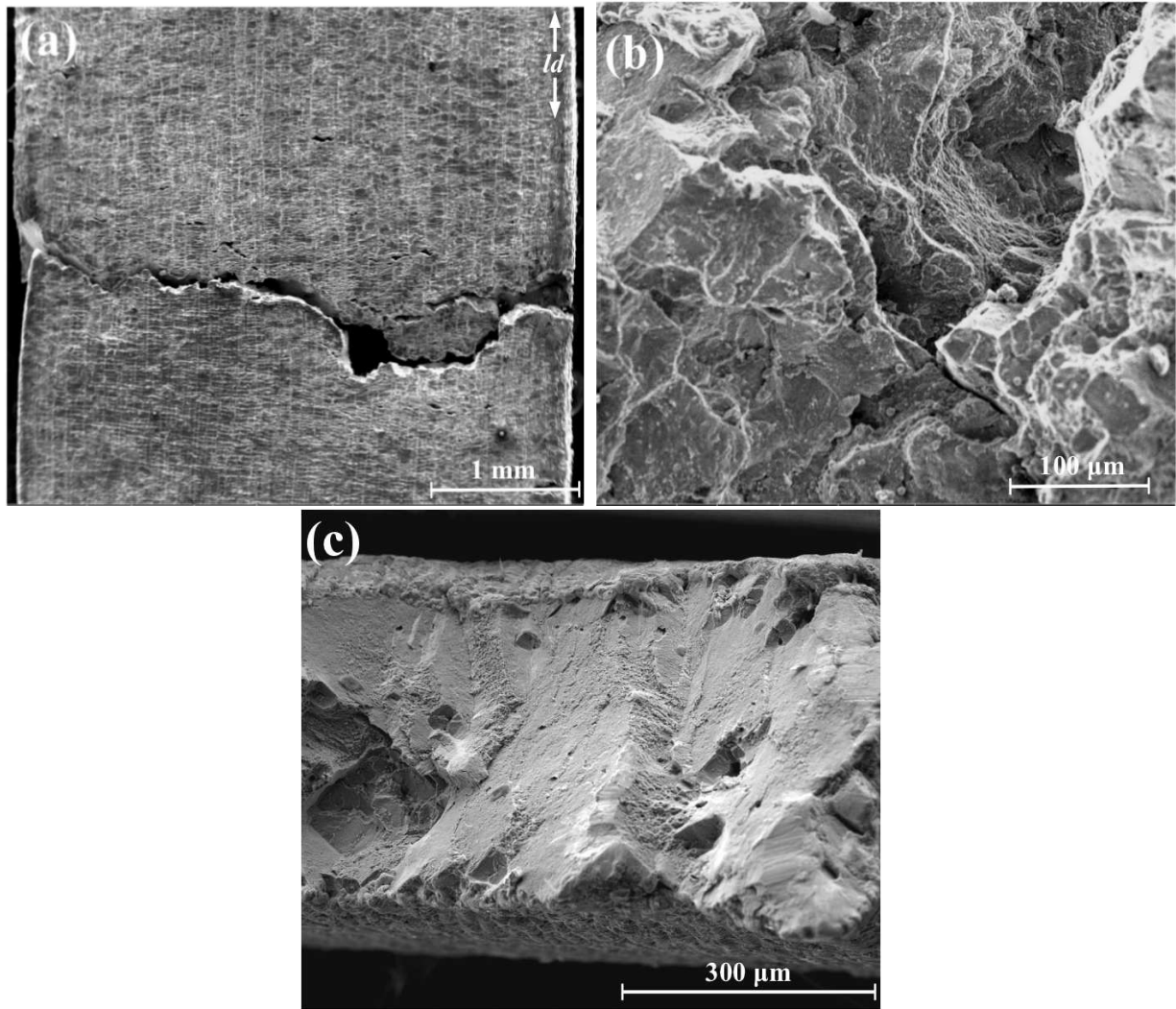


Figure 19: SEM images of a 0.51mm thick sheet specimen tested at 982°C/248MPa. (a) The region near the fracture surface reconstructed after rupture (the loading direction  $ld$  and the sheet thickness is into the plane). (b) A part of the fracture surface of the one half of the specimen in (a) (the loading direction is into the viewed plane). (c) The fracture morphology of one end of the specimen in (a) showing cleavage steps (the loading direction is into the viewed plane).

perpendicular to the loading direction in the gauge section away from the fracture surface as with  $h = 3.18\text{mm}$  can be seen. The fracture surface obtained with  $h = 0.51\text{mm}$  contains both dimple rupture and cleavage steps. The region of the fracture surface in Fig. 19b shows the presence of deformed micro-voids and irregular bulged areas. This type of fracture morphology is observed over a large fraction of the fracture surface. At both ends of the fracture surface in Fig. 19a, we can see the presence of cleavage steps as shown in Fig. 19c that are inclined to the loading direction. The region surrounding the voids on the cleavage plane are orthogonal to the loading direction. This indicates that the cleavage cracks perpendicular

to the loading axis initiated from voids and then propagated along crystallographic planes finally leading to rupture. The difference in the fracture morphology of specimens with thicknesses  $h = 0.51\text{mm}$  and  $h = 3.18\text{mm}$  can be related to the increased void nucleation for  $h = 3.18\text{mm}$  as shown in Fig. 17.

#### 4. Discussion

The thickness debit effect of sheet specimens of PWA1484 Ni-based single crystal superalloy has a distinctly different manifestation in the two creep test conditions considered. In the low temperature high stress creep condition ( $760^\circ\text{C}/758\text{MPa}$ ) the thickness debit effect has the form of a reduction in the creep strain to rupture and the time to rupture with decreasing specimen thickness. The fracture surfaces for the thinner specimens are more cleavage dominated and the creep strain versus time response exhibits little or no tertiary creep. The thickness debit effect at the high temperature low stress creep condition ( $982^\circ\text{C}/248\text{MPa}$ ) has the form of an increase in creep rate even at low creep strain levels and a reduction in the time to creep rupture with decreasing thickness but with no systematic dependence of the creep strain to rupture on specimen thickness.

The undeformed microstructure contains voids formed during the solidification and homogenization processes. These voids may serve as the preferred crack nucleation sites. Motivated by the present experimental results Srivastava and Needleman [50] carried out three dimensional finite deformation finite element cell model analyses of porosity evolution in an fcc single crystal under creep loading. The unit cell contains a single initially spherical void and the imposed stress state is characterized by the three principle stresses  $\Sigma_1$ ,  $\Sigma_2$  and  $\Sigma_3$  with  $\Sigma_1 \geq \Sigma_2 \geq \Sigma_3$ . Key parameters characterizing the stress state are the stress triaxiality, the ratio of Mises effective stress  $\Sigma_e$  to mean normal stress  $\Sigma_h$ , and the Lode parameter  $L$ .

The stress triaxiality  $\chi$  is given by

$$\chi = \frac{\Sigma_h}{\Sigma_e} \quad (1)$$

where

$$\Sigma_e = \frac{1}{\sqrt{2}} \sqrt{(\Sigma_1 - \Sigma_2)^2 + (\Sigma_2 - \Sigma_3)^2 + (\Sigma_3 - \Sigma_1)^2} \quad \Sigma_h = \frac{1}{3}(\Sigma_1 + \Sigma_2 + \Sigma_3) \quad (2)$$

The stress triaxiality is the ratio of the first to second stress invariants and is  $1/3$  for uniaxial tension.

The influence of the third stress invariant is assessed via the Lode parameter,  $L$ , which is given by

$$L = \frac{2\Sigma_2 - \Sigma_1 - \Sigma_3}{\Sigma_1 - \Sigma_3} \quad (3)$$

The value of the Lode parameter ranges from  $-1$  to  $+1$  with  $L = -1$  for uniaxial tension.

In [50], where calculations were carried out for relatively isolated voids, it was found that for stress triaxiality value of  $1/3$  and Lode parameter value of  $-1$  although creep led



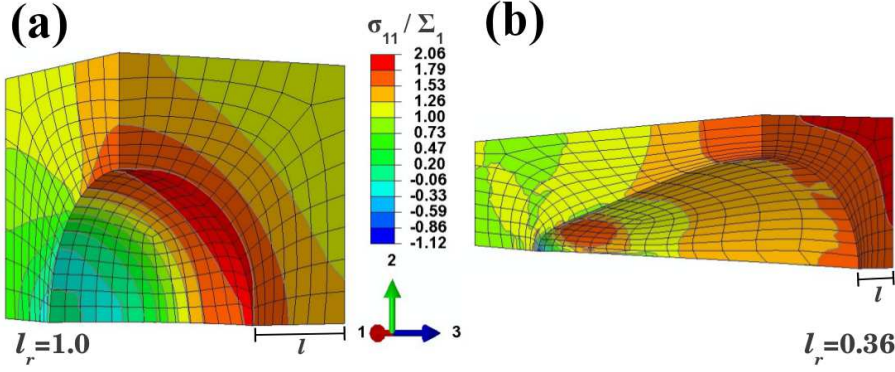


Figure 20: Distributions of normalized stress  $\sigma_{11}/\Sigma_1$  for tensile creep loading in the  $x_1$  direction. (a) At initial elastic loading where the ratio of current to initial ligament length,  $l_r = l/l_0$ , between two periodic voids is 1.0. (b) When the relative ligament is reduced to  $l_r = 0.36$ .

to an initial stress relaxation, the void shape change can lead to an increased local stress concentration. Under these conditions an isolated spherical void evolves into a needle-like shape without a significant increase in void volume and a stress concentration of 1.63 was found in [50]. For other values of Lode parameter void-collapse into a crack-like shape can occur and for  $\chi = 1/3$  and  $L = 1$  a stress concentration of 2.8 near the crack tip was found in [50]. A stress concentration can also develop in the ligament between two relatively closely spaced voids. Based on the formulation in [50] we carried out a calculation for  $\chi = 1/3$  and  $L = -1$  with the voids closely spaced (an initial half inter void ligament to radius ratio  $l_0/r_0$  of 0.74 as compared to  $l_0/r_0 = 2.74$  in [50]). Figure 20 shows the stress concentration ( $\Sigma_1$  is the applied stress and  $\sigma_{11}$  is the local normal stress in the direction of loading) in the ligament between voids in a creeping single crystal at two stages of deformation; Fig. 20(a) just after initial loading where the maximum stress concentration is 1.8 in a small region near the void surface; and Fig. 20(b) when the ligament between voids is reduced to 36% of its initial size and the stress concentration has increased to 2.06 and is nearly that value over the entire cross section. Although the specimen loading in the experiments corresponds to uniaxial tension local inhomogeneities can give rise to stress states in the vicinity of a void that has different values of  $\chi$  and/or  $L$ . For example, in a calculation with  $l_0/r_0 = 0.74$ ,  $\chi = 1/3$  and  $L = 1$  at  $l_r = 0.36$  the maximum stress concentration was about 3.

If stress concentration is large enough to precipitate cleavage, the resulting reduction of stress carrying capacity would be more adverse for thinner specimens thus giving rise to a thickness debit effect. The microstructural characterization of the specimens creep ruptured at 760°C/758MPa indeed showed tensile cracks extending from voids in the region perpendicular to the loading direction. These tensile cracks coalesce with shear cracks on the  $\{111\}$  planes which have the maximum resolved shear stress. Thus in the low temperature high stress condition, 760°C/758MPa, a stress concentration associated with the initial voids can precipitate nucleation of cleavage cracks so that the thickness debit effect is a bulk effect arising from the increased crack size to thickness ratio for thinner specimens.

At 982°C/248MPa, the microstructural characterization of both specimens where the tests were interrupted prior to rupture and ruptured specimens showed spallation of oxides and formation of an adherent Al-rich oxide layer. Surface oxidation led to the formation of a  $\gamma'$ -precipitate free and depleted zone as shown in Fig. 13. These precipitate free zones underwent dynamic recrystallization resulting in the formation of subgrains and recrystallized twins Fig. 16. Similar oxidation induced dynamic recrystallization of the near surface region during thermomechanical fatigue of CMSX-4 single crystal superalloy has been reported by Moverare and Johansson [51]. Surface recrystallization of single crystal superalloys has been generally observed in circumstances where the surface is predeformed via surface indentation [52] or shot peening [53]. In the absence of residual plastic strain and at a temperature well below the solvus temperature of  $\gamma'$  precipitate dynamic recrystallization is mainly due to the oxidation induced precipitate depletion. Xie et al. [54] studied the effect of heat treatment atmosphere at 1220°C and reported an increased recrystallization due to oxidation in the predeformed surface of directionally solidified superalloy.

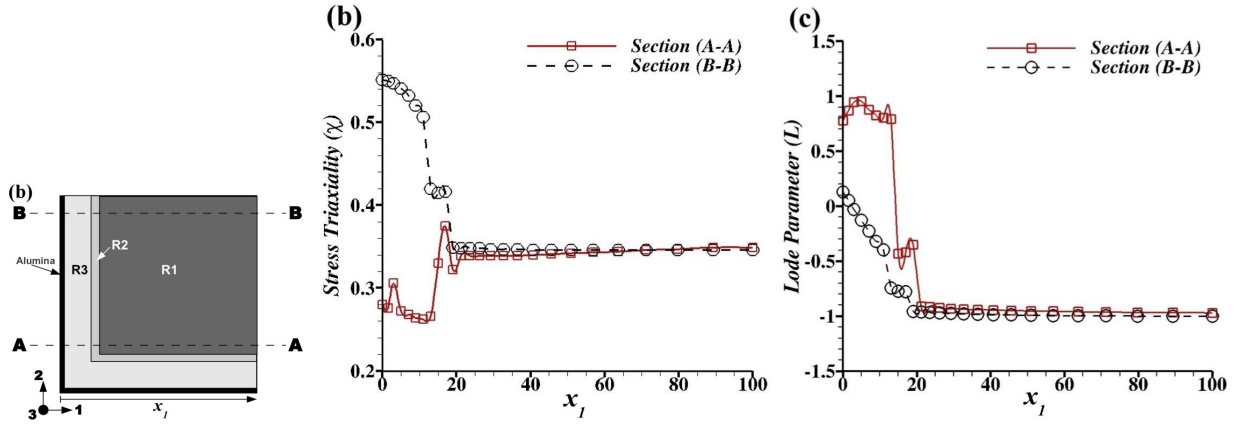


Figure 21: Computational results for the change in stress state near the free surface due to an adherent surface oxide and dynamic recrystallization for applied uniaxial creep loading in the  $x_3$ -direction giving  $\chi = 1/3$  and  $L = -1$ . (a) Sketch of the cross section of the configuration analyzed. (b) Variation of stress triaxiality  $\chi$  on two cuts. (c) Variation of the value of the Lode parameter  $L$  on two cuts.

Void nucleation and growth occurred throughout the specimen but predominantly in the recrystallized zone. An increased damage in the recrystallized zone during thermomechanical fatigue was also observed in [51]. Based on this observation a finite element analysis was carried out to estimate the change in stress state due to the presence of the adherent surface oxide and the layered structure that forms near the surface of the specimen tested at 982°C/248MPa. Figure 21(a) shows the schematic of the configuration analyzed. Region R1 represents the central bulk material, region R2 represents the  $\gamma'$  depleted region and R3 represents the  $\gamma'$  free region. The model cross section was taken to be  $100\mu\text{m} \times 100\mu\text{m}$ , region R3 was taken to be  $12\mu\text{m}$  and region R2 was taken to be  $6\mu\text{m}$  thick. The actual specimen cross section is of course much larger but the calculations show that the bulk state of uniform tension is attained a short distance away from the surface. Dimensions for this

calculation are given in  $\mu\text{m}$  but all that matters for the continuum finite element analysis is ratios of geometric lengths.

Finite element finite deformation calculations were carried out using the commercial program ABAQUS [55] using C3D20H elements (20 node hybrid elements) and symmetry conditions were imposed on the sides at  $x_1 = 100\mu\text{m}$  and  $x_2 = 100\mu\text{m}$ . Constant engineering stress creep loading, as in the experiments, was imposed in the  $x_3$  direction. The deformation was assumed uniform in the  $x_3$  direction so that only 5 layers of elements normal to the  $x_3$  direction were used. On one external plane normal to the loading direction  $u_3 = U$  is imposed for all nodes while  $u_3 = 0$  for all nodes on the opposite normal plane. The displacement  $u_1$  was taken to vanish on the external surface parallel to the  $x_1$  direction similarly  $u_2 = 0$  on the external surface parallel to the  $x_2$  direction in order to simulate the constrain imposed by the adherent alumina layer. Since the adherent alumina layer readily cracks normal to the loading direction we assume that it does not impose any constraint in the loading direction ( $x_3$  direction). All three regions were assumed to follow the isotropic Norton power law creep relation

$$\dot{\epsilon}_e = \dot{a} \left( \frac{\sigma_e}{\sigma_0} \right)^n \quad (4)$$

where  $\sigma_e$  is the Mises effective stress and  $\dot{\epsilon}_e$  is the corresponding effective strain rate. The appropriate creep properties for regions R2 and R3 are not known but it is expected that the creep rate increases with a decreasing volume of  $\gamma'$  as assumed in [37]. The parameters  $\sigma_0$  and  $n$  are chosen to exhibit this trend in creep rate and the reference strain rate  $\dot{a}$  is fixed at  $7.59 \times 10^{-8}\text{s}^{-1}$ . In region R1  $\sigma_0 = 150\text{MPa}$  and  $n = 5$ , in region R2  $\sigma_0 = 15\text{MPa}$  and  $n = 5$  and in region R3  $\sigma_0 = 6.92\text{MPa}$  with  $n = 7$ . Note that in Eq. 4 the values of  $\sigma_0$  and  $\dot{a}$  do not independently affect  $\dot{\epsilon}_e$ ; all that matters is the combination  $\dot{a}/\sigma_0^n$ . The elastic constants in region R1 was taken as  $C_{11} = 271\text{GPa}$ ,  $C_{12} = 194\text{GPa}$  and  $C_{44} = 105\text{GPa}$ , region R2 was assumed to be elastically isotropic with  $E = 210\text{GPa}$  and Poisson's ratio 0.3, and region R3 was also assumed to be elastically isotropic with  $E = 200\text{GPa}$  and Poisson's ratio 0.31. The calculations were continued to an engineering creep strain of 10%.

Figure 21(b) and (c) illustrates the change in stress state that can occur due to the development of a heterogeneous microstructure. Figure 21(b) shows the variation of stress triaxiality  $\chi$  and Fig. 21(c) shows the variation in Lode parameter  $L$  along the sections A-A and B-B. The constraint imposed on the free surface of the region R3 results in a decrease in stress triaxiality value near the corner and an increase in the value of  $\chi$  away from the corner. Away from the surface stress triaxiality  $\chi$  and Lode parameter  $L$  attain values corresponding to a uniaxial state of stress ( $\chi = 1/3$  and  $L = -1$ ). The variation of  $L$  in the regions R2 and R3 covers the entire range from  $-1$  to  $1$ . The analyses in [50] show that the evolution of porosity is a strong function of Lode parameter for moderate and low stress triaxiality values. This change in stress state will also affect the material response during thermomechanical fatigue.

At  $982^\circ\text{C}/248\text{MPa}$  the comparison of the accumulated damage in the form of microvoids and micro-cracks showed that the specimens of thickness  $3.18\text{mm}$  accumulated more microvoids and micro-cracks than the specimens of thickness  $0.51\text{mm}$ . This can be related

to the fracture morphology where a transition from homogeneous dimple rupture in the case of the thicker specimens to a mixed mode of void nucleation and growth together with cleavage for the thinner specimens was observed. This suggests that processes in the bulk also play a significant role in the thickness debit effect. Models such as those in [35, 36] have focused only on near surface processes as being responsible for the thickness debit effect. At 982°C/248MPa our experimental and modeling results indicate that the observed thickness debit effect involves both surface and bulk effects. The bulk processes are similar to those in the low temperature high stress condition while the surface effects include oxidation, formation of a boundary damage layer due to dynamic recrystallization and the change in stress state that occurs as a consequence of a change in near surface microstructure and properties. This surface degradation of the specimens is independent of the thickness and hence affects thinner specimens more than thicker ones.

## 5. Summary and conclusions

Isothermal, constant nominal stress creep tests at two test conditions 760°C/758MPa and 982°C/248MPa were performed on uncoated PWA1484 Ni-based single crystal super-alloy sheet specimens of thickness  $h = 3.18\text{mm}$  and  $h = 0.51\text{mm}$ . Metallographic studies showed that the specimens contained initial voids mainly in the interdendritic regions. To understand the contribution of various mechanisms possibly leading to the thickness debit effect, creep tests at 982°C/248MPa were interrupted after  $t = 75$  hours and  $t = 145.7$  hours for specimens of  $h = 3.18\text{mm}$  and after  $t = 51.2$  hours for specimen of  $h = 0.51\text{mm}$ . The dependence of the creep response on specimen thickness differed under the two test conditions:

- Low temperature high stress condition (760°C/758MPa):
  1. There was little effect of specimen thickness on the steady-state creep rate. The main effect of specimen thickness was on the onset of tertiary creep and for  $h = 0.38\text{mm}$  failure occurred prior to any tertiary creep.
  2. A decrease in specimen thickness from 3.18mm to 0.38mm resulted in over 40% reduction in the creep strain to rupture and around a 60% reduction in the time to rupture.
  3. Neither oxide formation on the specimen surfaces, rafting nor void nucleation was observed.
  4. With  $h = 3.18\text{mm}$  a mixed mode of failure involving ductile void growth and coalescence and cleavage cracking was observed. With  $h = 0.51\text{mm}$  cleavage cracking covered more of the failure surface.
  5. The thickness debit effect can be attributed to the following process: the change in void shape with increasing deformation leads to an enhanced stress concentration that triggers cleavage. The loss in load carrying area due to cleavage cracking raises the stress level on the remaining intact surface which promotes

additional cleavage. The deleterious effect of loss of intact area is greater for thinner specimens.

- High temperature low stress condition (982°C/248MPa):

1. The steady-state creep rate increased with decreasing specimen thickness. The time to reach 5% creep strain was reduced by 18% for the specimens with thickness  $h = 0.51\text{mm}$  as compared with the specimens with  $h = 3.18\text{mm}$ .
2. The time to rupture for the specimens with  $h = 0.51\text{mm}$  was 25% less than that for the specimens with  $h = 3.18\text{mm}$  but there was no systematic dependence of the strain to rupture on specimen thickness.
3. Surface oxides formed. Spallation of the Ni-rich and mixed oxide layers and formation of adherent Al-rich oxide was observed. Cracks formed in the adherent oxide layer exposed metal but were arrested due to further oxidation.
4. Oxidation of the uncoated specimens resulted in the formation of a  $\gamma'$ -precipitate free zone. The precipitate free zone underwent dynamic recrystallization resulting in the formation of subgrains.
5. Void nucleation was observed throughout the specimen and particularly in the precipitate free zone.
6. Finite element analysis of a constrained layered structure shows a near surface increase in stress triaxiality and a change in Lode parameter.
7. A transition from homogeneous dimple fracture due to void nucleation, growth and coalescence to a mixed mode of void nucleation, growth and coalescence together with cleavage was observed with decreasing specimen thickness.

Our results show that, depending on temperature and stress magnitude, bulk and surface mechanisms can play a role in the thickness debit effect. This is also the case for room temperature plastic deformation with, depending on circumstances, geometrically necessary dislocations (a bulk effect) and/or source truncation and dislocation starvation (where surfaces are involved) leading to a size effect.

## Acknowledgments

We are grateful for the financial support provided by the Air Force Research Laboratory (AFRL/RXLM) to the University of North Texas under the Institute for Science and Engineering Simulation (ISES) Contract FA8650-08-C-5226.

## References

- [1] Gell M., Duhl D.N. and Giamei A.F. The development of single crystal superalloy turbine blades. *Superalloys* 1980, 205-214.
- [2] Koff B.L. Gas turbine technology evolution: A designers perspective. *Journal of Propulsion and Power*, 2004, 20, 577595.

- [3] Pandey M.C., Dyson B.F. and Taplin D.M.R. Environmental, Stress-State and Section-size synergisms During Creep. *Proc. R. Soc. Lond., Ser. A*, 1984, 117-131.
- [4] Doner M. and Heckler J.A. Effects of section thickness and orientation on creep rupture properties of two advanced single crystal alloys. SAE technical paper 851785, (Society of Automotive Engineers Inc.), 1985.
- [5] Duhl D.N. Directionally solidified superalloys, in *Superalloys II*, C.T. Sims, N.S. Stoloff, and W.C. Hagel, (Eds.), (John Wiley, New York), 1987, 189-214.
- [6] Doner M. and Heckler J.A. Identification of mechanism responsible for degradation in thin-wall stress rupture properties. *Superalloys 1988*, Proceedings of the 6<sup>th</sup> international symposium on superalloys, The metallurgical society, Warrendale, PA, 1988, 653-662.
- [7] Duhl D.N. Single crystal superalloys, *Superalloys, Supercomposites and Superceramics*, J.K. Tien and T. Caulfield (Eds.), Academic Press, Inc. New York, NY, 1989, 149-182.
- [8] Pandey M.C. and Taplin D.M.R. Prediction of rupture lifetime in thin sections of a nickel base superalloy. *Scripta Metallurgica et Materialia*, 1994, 31, 719-722.
- [9] Baldan A. On the thin-section size dependent creep strength of a single crystal nickel-base superalloy. *Journal of materials science*, 1995, 30, 6288-6298.
- [10] Henderson P.J. Creep of single crystal Ni-base superalloy in thick and thin section forms. *Creep and fracture of engineering materials and structures*, ed. J.C. Earthman and F.A. Mohamed, 1997, 697-706.
- [11] Seetharaman V. and Cetel A.D. Thickness Debit in Creep Properties of PWA1484. *Superalloys 2004*, TMS (The Minerals, Metals and Materials Society), 2004, 207-214.
- [12] Henderson P.J. Creep of coated and uncoated thin-section CMSX-4. *Materials for advanced power engineering*, (Forschungszentrum Juelich GmbH), 1998, 1559-1568.
- [13] Hüttner R., Völkl R., Gabel J. and Glatzel U. Creep behavior of thick and thin walled structures of a single crystal Ni-base superalloy at high temperatures-Experimental method and results. *Superalloys 2008*, R.C. Reed, K.A. Green, P. Carron, T.P. Gabb, M.G. Fahrman, E.S. Huron and S.A. Woodard, TMS (The Minerals, Metals and Materials Society), 2008, 719-723.
- [14] Hüttner R., Gabel J., Glatzel U. and Völkl R. First creep results on thin-walled single-crystal superalloys. *Material science and engineering A*, 2009, 510-511, 307-311.
- [15] Cetel A.D. and Duhl D.N. Second Generation Nickel Base Single Crystal Superalloy. *Superalloys 1988*, Proceedings of the 6th International Symposium on Superalloys, The Metallurgical Society, Warrendale, PA, 1988, 235-244.
- [16] Cane B.J. and Townsend R.D. Prediction of Remaining Life in Low-alloy Steels. In: Raj R. (Ed.), *Flow and Fracture at Elevated Temperatures*, pp. 279-316. American Society of Metals, Metals Park, Ohio 44703, USA.
- [17] Storesund J. and Tu S.T. Geometrical effect on creep in cross weld specimens. *Int. J. Pres. Ves. & Piping*, 1995, 62, 179-193.
- [18] Ueno A., Takami N. and Sato R. In: J. Pokluda (Ed.), *Proceedings of the 17th European Conference of Fracture*, Brno, Czech Republic, 2008, pp. 1120-1127.
- [19] Villain J., Brueller O.S. and Qasim T. Creep behaviour of lead free and lead containing solder materials at high homologous temperatures with regard to small solder volumes. *Sensors and Actuators A*, 2002, 99, 194-197.
- [20] Ashby, M.F. The deformation of plastically non-homogeneous materials. *Philosophical Magazine*, 1970, 21, 399-424.
- [21] Ma, Q., Clarke, D.R. Size dependent hardness of silver single crystals. *Journal of Materials Research*, 1995, 10, 853863.
- [22] Lou, J., Shrotriya, P., Buchheit, T., Yang, D., Soboyejo, W.O. Nanoindentation study of plasticity length scale effects in LIGA Ni microelectromechanical systems structures. *Journal of Materials Research*, 2003, 18, 719728.
- [23] Poole, W.J., Ashby, M.F., Fleck, N.A. Micro-hardness of annealed and work-hardened copper

- polycrystals. *Scripta Materialia*, 1996, 34, 559564.
- [24] Nix, W.D., Gao, H. Indentation size effects in crystalline materials: a law for strain gradient plasticity. *Journal of the Mechanics and Physics of Solids*, 1995, 43, 411423.
  - [25] Uchic, M.D., Dimiduk, D.M., Florando, J.N., Nix, W.D. Sample dimensions influence strength and crystal plasticity. *Science*, 2004, 305, 986989.
  - [26] Greer, J.R., Oliver, W.C., Nix, W.D. Size dependence of mechanical properties of gold at the micron scale in the absence of strain gradients. *Acta Materialia*, 2005, 53, 1821-1830.
  - [27] L. Nicola, Y. Xiang, J.J. Vlassak, E. Van der Giessen and A. Needleman. Plastic deformation of freestanding thin films: experiments and modeling. *Journal of the Mechanics and Physics of Solids*, 2006, 54, 2089-2110.
  - [28] Kiener, D., Guruprasad, P.J., Keralavarma, S.M., Dehm, G., Benzerga, A.A. Work hardening in micropillar compression: In situ experiments and modeling, *Acta Materialia*, 2011, 59, 3825-3840.
  - [29] Benzerga, A.A. Micro-pillar plasticity: 2.5D mesoscopic simulations. *Journal of the Mechanics and Physics of Solids*, 2009, 57, 1459-1469.
  - [30] Rao, S.I., Dimiduk, D.M., Parthasarathy, T.A., Uchic, M.D., Tang, M., Woodward, C. Athermal mechanisms of size-dependent crystal flow gleaned from three-dimensional discrete dislocation simulations. *Acta Materialia*, 2008, 3245-3259
  - [31] Kraft, O., Gruber, P.A., Mönig, R., Weygand, D. Plasticity in confined dimensions. *Annual Review of Materials Research*, 2010, 40, 293-317.
  - [32] Greer, J.R., Fe Hosson, J.Th.M. Plasticity in small-sized metallic systems: intrinsic versus extrinsic size effect. *Progress in Materials Science*, 2011, 56, 654-724.
  - [33] Zupan, M., Hayden, M.J., Boehlert, C.J., Hemker, K.J. Development of high temperature microsample testing. *Experimental Mechanics*, 2001, 41, 242247.
  - [34] K.J. Hemker and W.N. Sharpe, Jr. Microscale Characterization of Mechanical Properties. *Annual Reviews of Materials Research*, 2007, 37, 93-126.
  - [35] Gullickson J., Needleman A., Staroselsky A. and Cassenti B. Boundary damage effects on the evolution of creep strain. *Modelling and Simulation in Materials Science and Engineering*, 2008, 16, 075009.
  - [36] Cassenti B. and Staroselsky A. The effect of thickness on the creep response of thin-wall single crystal components. *Materials Science and Engineering A*, 2009, 508, 183-189.
  - [37] Bensch M., Preußner J., Hüttner R., Obigodi G., Virtanen S., Gabel J. and Glatzel U. Modelling and analysis of the oxidation influence on creep behaviour of thin-walled structures of the single-crystal nickel-base superalloy René N5 at 980°C. *Acta Materialia*, 2010, 58, 1607-1617.
  - [38] Duhl D.N. and Cetel A.D. Advanced high strength single crystal superalloy compositions, U.S. Patent 4719080, January 12, 1988.
  - [39] Anton D.L. and Giamei A.F. Porosity distribution and growth during homogenization in single crystals of a nickel-base superalloy. *Materials Science and Engineering*, 1985, 76, 173-180.
  - [40] Link T., Zabler S., Epishin A., Haibel A., Bansal M. and Thibault X. Synchrotron tomography of porosity in single-crystal nickel-base superalloys. *Materials Science and Engineering A*, 2006, 425, 47-54.
  - [41] Wilson B. and Fuchs G. Primary creep: secondary gamma prime and the rhenium effect. *JOM Journal of the Minerals, Metals and Materials Society*, 2008, 60, 43-48.
  - [42] Sherry A.H. and Pilkington R. The creep fracture of a single-crystal superalloy. *Materials Science and Engineering A*, 1993, 173, 51-61.
  - [43] ASM Handbook, Fractography, Volume 12, 1987.
  - [44] Mennicke C., He M.Y., Clarke D.R. and Smith J.S. The role of secondary oxide inclusions ("PEGS") on the spalling resistance of oxide films. *Acta Materialia*, 2000, 48, 2941-2949.
  - [45] Nychka A.J., Clarke D.R. and Meier G.H. Spallation and transient growth on PWA1484 superalloy. *Material Science and Engineering A*, 2008, 490, 359-368.

- [46] MacKay R.A. and Ebert L.J. The development of  $\gamma - \gamma'$  lamellar structures in a Ni-base superalloy during elevated temperature mechanical testing. *Metallurgical Transactions A*, 1985, 16A, 1969-1982.
- [47] Sato A., Chiu Y.L. and Reed R.C. Oxidation of nickel-based single crystal superalloys for industrial gas turbine applications. *Acta Materialia*, 2011, 59, 225-240.
- [48] Akhtar A., Hegde S. and Reed R.C. The oxidation of single-crystal nickel-based superalloys. *JOM Journal of the Minerals, Metals and Materials Society*, 2006, 58, 37-42.
- [49] Epishin A. and Link T. Mechanisms of high-temperature creep of nickel-based superalloys under low applied stresses. *Philosophical Magazine*, 2004, 84, 1979-2000.
- [50] Srivastava A. and Needleman A. Porosity evolution in a creeping single crystal. *Modelling and Simulation in Materials Science and Engineering*, 2012, 20, 035010.
- [51] Moverare J.J. and Johansson S. Damage mechanisms of a high-Cr single crystal superalloy during thermomechanical fatigue. *Materials Science and Engineering: A*, 2010, 527, 553-558.
- [52] Bond S.D. and Martin J.W. Surface recrystallization in a single crystal nickel-based superalloy. *Journal of Materials Science*, 1984, 19, 3867-72.
- [53] Meng J., Jin T., Sun X. and Hu Z. Surface recrystallization of a single crystal nickel-base superalloy. *International Journal of Minerals, Metallurgy and Materials*, 2011, 18, 197-202.
- [54] Xie G., Zhang J. and Lou L.H. Effect of heat treatment atmosphere on surface recrystallization of a directionally solidified Ni-base superalloy. *Scripta Materialia*, 2008, 59, 858-861.
- [55] ABAQUS User's Manual, version 6.6, 2006, ABAQUS Inc., Providence, RI.